



HAL
open science

HR-GO

T M Sitnova, Z Yuan, T Matsuno, L I Mashonkina, S A Alexeeva, E Holmbeck, F Sestito, L Lombardo, P Banerjee, N F Martin, et al.

► **To cite this version:**

T M Sitnova, Z Yuan, T Matsuno, L I Mashonkina, S A Alexeeva, et al.. HR-GO. Astronomy and Astrophysics - A&A, 2024, 690, 10.1051/0004-6361/202450981 . insu-04756719

HAL Id: insu-04756719

<https://insu.hal.science/insu-04756719v1>

Submitted on 28 Oct 2024

HAL is a multi-disciplinary open access archive for the deposit and dissemination of scientific research documents, whether they are published or not. The documents may come from teaching and research institutions in France or abroad, or from public or private research centers.

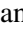



L'archive ouverte pluridisciplinaire **HAL**, est destinée au dépôt et à la diffusion de documents scientifiques de niveau recherche, publiés ou non, émanant des établissements d'enseignement et de recherche français ou étrangers, des laboratoires publics ou privés.



Distributed under a Creative Commons Attribution 4.0 International License

HR-GO

I. Comprehensive NLTE abundance analysis of the Cetus stream

T. M. Sitnova^{1,*}, Z. Yuan^{2,3,4,*}, T. Matsuno⁵, L. I. Mashonkina¹ , S. A. Alexeeva⁶ , E. Holmbeck⁷,
F. Sestito⁸ , L. Lombardo⁹ , P. Banerjee¹⁰, N. F. Martin⁴, and F. Jiang^{11,7}

¹ Institute of Astronomy, Russian Academy of Sciences, Pyatnitskaya 48, 119017 Moscow, Russia

² School of Astronomy and Space Science, Nanjing University, Nanjing 210093, China

³ Key Laboratory of Modern Astronomy and Astrophysics (Nanjing University), Ministry of Education, Nanjing 210093, China

⁴ Université de Strasbourg, CNRS, Observatoire astronomique de Strasbourg, UMR 7550, 67000 Strasbourg, France

⁵ Astronomisches Rechen-Institut, Zentrum für Astronomie der Universität Heidelberg, Mönchhofstraße 12-14, 69120 Heidelberg, Germany

⁶ CAS Key Laboratory of Optical Astronomy, National Astronomical Observatories, Chinese Academy of Sciences, Beijing 100101, China

⁷ The Observatories of the Carnegie Institution for Science, 813 Santa Barbara Street, Pasadena, CA 91101, USA

⁸ Department of Physics and Astronomy, University of Victoria, PO Box 3055, STN CSC, Victoria BC V8W 3P6, Canada

⁹ Goethe University Frankfurt, Institute for Applied Physics (IAP), Max-von-Laue-Str. 12, 60438 Frankfurt am Main, Germany

¹⁰ Department of Physics, Indian Institute of Technology Palakkad, Kerala 678558, India

¹¹ Kavli Institute for Astronomy and Astrophysics, Peking University, Beijing 100871, China

Received 4 June 2024 / Accepted 13 August 2024

ABSTRACT

Context. Dwarf galaxy streams encode vast amounts of information essential to understanding early galaxy formation and nucleosynthesis channels. Due to the variation in the timescales of star formation history in their progenitors, stellar streams serve as ‘snapshots’ that record different stages of galactic chemical evolution.

Aims. This study focusses on the Cetus stream, stripped from a low-mass dwarf galaxy. We aim to uncover its chemical evolution history as well as the different channels of its element production from detailed elemental abundances.

Methods. We carried out a comprehensive analysis of the chemical composition of 22 member stars based on their high-resolution spectra. We derived abundances for up to 28 chemical species from C to Dy and, for 20 of them, we account for the departures from local thermodynamic equilibrium (NLTE effects).

Results. We confirm that the Cetus stream has a mean metallicity of $[Fe/H] = -2.11 \pm 0.21$. All observed Cetus stars are α enhanced with $[\alpha/Fe] \approx 0.3$. The absence of the α -‘knee’ implies that star formation stopped before iron production in type Ia supernovae (SNe Ia) became substantial. Neutron capture element abundances suggest that both the rapid (r-) and the main slow (s-) processes contributed to their origin. The decrease in $[Eu/Ba]$ from a typical r-process value of $[Eu/Ba] = 0.7-0.3$ with increasing $[Ba/H]$ indicates a distinct contribution of the r- and s-processes to the chemical composition of different Cetus stars. For barium, the r-process contribution varies from 100 to 20% in different sample stars, with an average value of 50%.

Conclusions. Our abundance analysis indicates that the star formation in the Cetus progenitor ceased after the onset of the main s-process in low- to intermediate-mass asymptotic giant branch stars but before SNe Ia played an important role. A distinct evolution scenario is revealed by comparing the abundances in the Ursa Minor dwarf spheroidal galaxy, showing the diversity in – and uniqueness of – the chemical evolution of low-mass dwarf galaxies.

Key words. stars: abundances – Galaxy: halo

1. Introduction

Ancient stars, which contain very small amounts of metals – typically less than one percent of the solar value –, encode vast amounts of information about the very early Universe. The studies of these old and low-metallicity stars belong to the field of Galactic archaeology (Spite & Spite 1979). In the *Gaia* era (Gaia Collaboration 2021), a library of stellar streams is being built, which are mainly populated by old stars (see e.g. Ibata et al. 2021; Li et al. 2022; Martin et al. 2022a; Ibata et al. 2024). These streams are the debris of ancient stellar systems, such as the globular clusters and dwarf galaxies that merged with the Milky Way (MW) during its long assembly history.

Among them, dwarf galaxy streams have unique value. Because of the relatively short star formation histories of their progenitors, the elemental abundances of the member stars are very sensitive to the initial mass function, star-forming activities, and chemical enrichment from different nucleosynthesis channels. Therefore, they serve as pristine laboratories for studying these physical processes that shaped the Universe we see today, and the elemental abundances of their member stars are the key to decoding such information. With modern large telescopes accompanied by high-resolution (HR) spectrographs, we are able to determine detailed abundances using high-quality stellar spectra. In this context, stellar streams from now-disrupted dwarf galaxies offer a great advantage over intact dwarf galaxies: streams are much closer to than the surviving dwarf galaxies with similar progenitor masses. This is the natural outcome of

* Corresponding authors: sitamih@gmail.com;
zhen.yuan@nju.edu.cn

hierarchical formation. Consequently, we have larger samples of bright stars from stellar streams for which high-quality HR spectra are attainable. Moreover, the observation efficiency for individual stars is greatly enhanced as the brightness increases.

Several recent works demonstrated the power of this approach and revealed the nature of the progenitors from the chemical composition of their stellar streams and substructures. Some of those streams arise from globular clusters, such as Typhon (Ji et al. 2023), ATLAS, Aliqa Uma, Phoenix (Ji et al. 2020a), GD-1 (Balbinot et al. 2022), C-19 (Martin et al. 2022b), and ω Cen stream (Gull et al. 2021), while others are from dwarf galaxies: Chenab, Elqui, Indus, Jhelum (Ji et al. 2020a), Helmi/S2 (Roederer et al. 2010; Limberg et al. 2021; Gull et al. 2021; Matsuno et al. 2022a), *Gaia* Sausage/Enceladus (Aguado et al. 2021; Ceccarelli et al. 2024), Sequoia (Aguado et al. 2021; Matsuno et al. 2022b; Ceccarelli et al. 2024), Wukong/LMS-1 (Limberg et al. 2024), Orphan-Chenab (Hawkins et al. 2023), and Specter, which formed from an ultrafaint dwarf (UFD) galaxy (Chandra et al. 2022); for some streams, their progenitor nature is debated: for example, Sylgr (Roederer & Gnedin 2019), Nyx (Wang et al. 2023), Antaeus, and ED-2 (Ceccarelli et al. 2024).

This study is conducted within a novel High-Resolution spectroscopic program on the Galactic Origins of elements (HR-GO) initiated by Z. Yuan. A detailed introduction to HR-GO will be given in a forthcoming paper (Yuan et al., in preparation). This program focusses on stars in stellar streams and substructures that are stripped from accreted dwarf galaxies. The goal is to understand the production channels of elements in dwarf galaxies as well as their evolution histories by observing stars in their debris. In the analysis procedure, we aim to obtain accurate stellar atmosphere parameters and detailed chemical compositions, accounting for the departures from local thermodynamic equilibrium (i.e. NLTE effects). This paper, as the first in this series of studies, reveals the detailed abundances of the Cetus stream for the first time.

The Cetus stream was discovered by Newberg et al. (2009) from ancient star tracers, blue straggler and blue horizontal branch stars in the Sloan Digital Sky Survey (SDSS, York et al. 2000). After *Gaia* DR2, using stellar orbits, Yuan et al. (2019) identified about 150 members from the K giant sample selected by Liu et al. (2014) from the Large Sky Area Multi-Object Fiber Spectroscopic Telescope survey (LAMOST, Cui et al. 2012; Deng et al. 2012; Zhao et al. 2012). To understand the disruption history in the MW potential, Chang et al. (2020) performed a series of N-body simulations and predicted a vast extension of the stream towards the south, surprisingly coincident with the Palca stream (Shipp et al. 2018). Later on, Thomas & Battaglia (2022) revealed that the Palca and Cetus streams are two parts of one stream and named it the Cetus-Palca stream. At about the same time, Yuan et al. (2022) found that the Cetus stream system has two wraps with different orbital phases, one of which contains the Palca stream and was thus named the Cetus-Palca wrap, while the other contains the Cetus stream, and was named the Cetus-New wrap.

All of the above studies give us a coherent picture of the Cetus progenitor system. It is mainly populated by very metal-poor (VMP, $[\text{Fe}/\text{H}]^1 < -2$) stars and has an average metallicity of -2.1 with an intrinsic dispersion of 0.2 dex in both

hemispheres, based on low-resolution spectroscopic and narrow-band photometric surveys (Newberg et al. 2009; Yam et al. 2013; Yuan et al. 2019, 2022). According to the stellar mass–metallicity relationship of the MW satellite dwarf galaxies (Kirby et al. 2013), the Cetus progenitor is compatible with a low-mass dwarf galaxy with a stellar mass of $M_* \gtrsim 10^6 M_\odot$. By summing the fluxes of all identified members, the Cetus progenitor is estimated to have a stellar mass of $M_* \gtrsim 10^{5.6} M_\odot$ (Yuan et al. 2022), which is similar to the Ursa Minor (UMi) dwarf spheroidal (dSph) galaxy ($M_* \sim 10^{5.7} M_\odot$) and Sextans dSph with $M_* \sim 10^{5.8} M_\odot$ (Kirby et al. 2013).

To reconstruct the history of chemical element formation in a given system, high-quality spectra are required, enabling the measurement of the detailed chemical composition, including α -elements, iron-peak elements, and neutron capture elements. The orbits of stars in the Cetus stream span a distance range from 10 to 40 kpc (Chang et al. 2020), making its giant stars perfect targets for high-resolution spectroscopic studies of chemical abundances. For comparison, the UMi dSph is located at a distance of 69 kpc (Mighell & Burke 1999). For UMi stars with V magnitudes from 16.7 to 17.2, Sadakane et al. (2004) took exposures of 150–210 minutes to obtain spectra with signal-to-noise ratios of 50–60 in the red wavelength region using the High Dispersion Spectrograph at the Subaru telescope. With the same instrument, exposures of only 30 minutes are needed to obtain spectra of the same quality for the Cetus stars with $V \approx 15$.

The paper is constructed as follows. We describe our target stars and the observations in Sect. 2. Section 3 presents a determination of stellar atmosphere parameters. The abundance determination method is described in Sect. 4. In Sect. 5, we present the comparison sample stars. The element abundances are given in Sect. 6 along with a discussion of our findings. Our conclusions are presented in Sect. 7.

2. Stellar sample and observations

Combining the member lists in Yuan et al. (2019) and Yuan et al. (2022), we select all the Cetus stars brighter than $G = 16$, yielding 22 stars in total for high-resolution spectroscopic follow up. According to Yuan et al. (2022), the main Cetus stream can be decomposed into two wraps (Cetus-Palca and Cetus-New), which have different orbital phases. In the HR target list, there are 12 stars from the Cetus-Palca wrap and 10 from the Cetus-New wrap denoted in Fig. 1 as blue and magenta circles, respectively. Although the on-sky projections of these two wraps overlap, they can be distinguished in the (b, d) and (b, v_{gsr}) spaces where b is the galactic latitude, d is the heliocentric distance, and v_{gsr} is the Galactic rest-frame radial velocity. These are the two signature spaces that best reveal the properties of the Cetus stream, as shown in Newberg et al. (2009), Yam et al. (2013), Yuan et al. (2019), and Yuan et al. (2022). The distances used in this work are derived from $\log g$, which are determined iteratively from *Gaia* parallax, photometry, and HR spectra, as described in Sect. 3. For each HR target, we trace its orbit backward and forward for about one-quarter of its period time and clearly see that stars in these two wraps follow distinct tracks, indicating that they are at different orbital phases. The orbital tracks of the Cetus-Palca wrap (solid blue line) exhibit a decreasing trend in d as b increases, and the Cetus-New wrap (solid magenta line) shows an opposite trend. Similarly, we can see that stars belonging to these two wraps follow different tracks in the (b, v_{gsr}) space.

¹ We use a standard designation, $[\text{X}/\text{Y}] = \log(N_{\text{X}}/N_{\text{Y}})_* - \log(N_{\text{X}}/N_{\text{Y}})_\odot$, where N_{X} and N_{Y} are total number densities of elements X and Y, respectively.

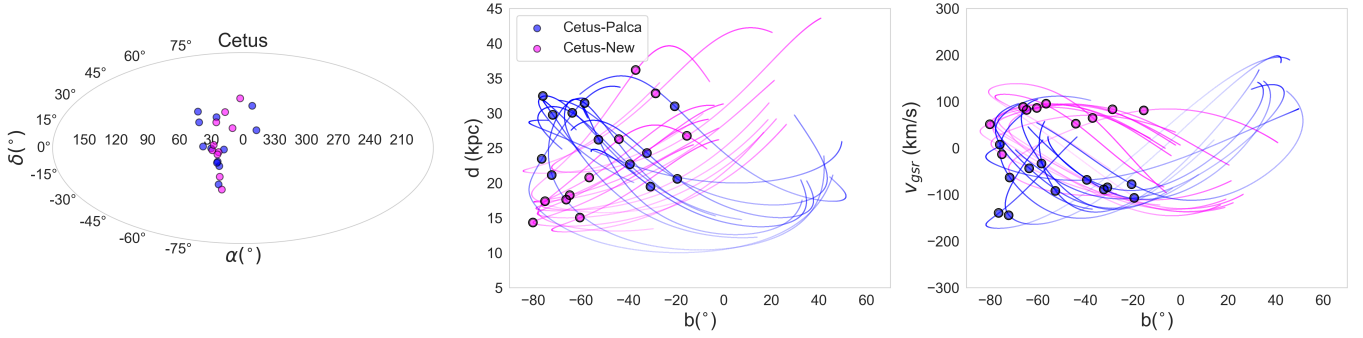


Fig. 1. Cetus stream members in the HR-GO program are shown in the (α, δ) and (b, d, v_{gsr}) space. The members belonging to the Cetus-Palca and Cetus-New wraps are denoted by blue and magenta circles, respectively. These two wraps have different orbital phases revealed by the integrated orbits of their member stars in the (b, d) and (b, v_{gsr}) spaces.

The high-resolution spectra of the 22 selected Cetus stars were taken in three observational programs with different telescopes and spectrographs and were processed with the corresponding pipelines:

1. The UV-visual echelle spectrograph (UVES) at the UT2 Kueyen Telescope on 23–24 October 2021 via program 0108.B-0431(A) (PI: Z. Yuan). The UVES spectra are derived with the 1.0'' slit width, which provides a resolving power of $R = \lambda/\Delta\lambda \sim 40\,000$. The wavelength coverage is 3750–5000, 5700–7500, and 7660–9450 Å (Dekker et al. 2000). The observed spectra are reduced with the ESO pipeline².
2. The Magellan Inamori Kyocera Echelle (MIKE) spectrograph at the Magellan Telescope on 19 August 2022 (PI: F. Jiang). The MIKE spectra are taken with the 0.7'' slit width, which yields $R \sim 28\,000$ and $\sim 35\,000$ in the red and blue wavelength regions, respectively (Bernstein et al. 2003). The wavelength coverage is 3300–9600 Å. The data reduction is carried out with the MIKE Carnegie Python pipeline (Kelson 2003). The barycentric velocity correction was performed using the online interface³, developed by Wright & Eastman (2014).
3. The High Dispersion Spectrograph (HDS) at the Subaru Telescope on 21 September 2022 via program S22B-0094N (PI: Z. Yuan). The HDS spectra are derived using the standard StdYd setup, which provides a wavelength coverage of 4000–5340 and 5450–6800 Å, with $R = 45\,000$ (Noguchi et al. 2002). The data were reduced using the IRAF⁴ script hdsq1⁵, which includes CCD linearity correction, scattered light subtraction, aperture extraction, flat-fielding, wavelength calibration, and barycentric velocity correction.

We list the coordinates, *Gaia* IDs, and characteristics of all target stars in Table 1. Observation information is also provided, including the telescope and spectrograph, the exposure time, and the resulting signal-to-noise ratio in the blue and red wavelength regions (S/N_B and S/N_R), corresponding to wavelengths around $\lambda \sim 4500$ Å and 6000 Å, respectively. We provide the S/N per pixel, which is calculated as the ratio between the mean

normalised flux (F_{mean}), which nearly equals unity, and its standard deviation $\sigma = \sqrt{\sum(F_{\text{mean}} - F_i)^2/(N - 1)}$, where F_i and N are the flux at a given wavelength and the number of data points in the selected spectral region, respectively. It is worth noting that spectra obtained with different instruments are characterised by a different number of pixels per resolving element. For our UVES, MIKE, and HDS spectra, a wavelength interval of 1 Å falls on 55, 50, and 70 pixels in the blue range, and on 40, 20, and 55 pixels in the red range, respectively.

To ensure the absence of systematic differences in our abundance analysis arising from the use of spectral observations obtained with different instruments, we observed star *Gaia* DR3 2505061738639700608 using both MIKE and HDS. Figure 2 presents a comparison of the equivalent widths (EWs) and abundances from iron lines measured from the two spectra. We find consistent EWs, with an average difference of $\Delta \text{EW}_{\text{HDS-MIKE}} = -4 \pm 8 \text{ mÅ}$, which translates to an average abundance difference of $-0.08 \pm 0.16 \text{ dex}$. For the majority of spectral lines in this star, we use its MIKE spectrum.

With our high-resolution spectra, we measure radial velocities (v_r , Table 1) with an uncertainty of 1 km s⁻¹. For the majority of the stars of our sample, our measurements are consistent with those provided in the *Gaia* DR3 catalogue. The exception is *Gaia* DR3 2507540140928136832, for which we find $v_r = -68.0 \pm 1 \text{ km s}^{-1}$, while *Gaia* provides $-88.68 \pm 9.98 \text{ km s}^{-1}$ and a renormalised unit weight error of $\text{RUWE} = 1.035$. We assume this star could be a binary.

3. Stellar parameters

Atmospheric parameters were derived through an iterative procedure. They are presented in Fig. 3 and Table 1. First, we calculate effective temperatures (T_{eff}) using the *Gaia* BP – G, G – RP, BP – RP dereddened colours and the calibration of Mucciarelli et al. (2021). The extinction $E(B - V)$ is adopted from Schlafly & Finkbeiner (2011) and the colours are corrected according to Casagrande & VandenBerg (2018). Using different colours yields very similar effective temperatures and the uncertainty in T_{eff} is therefore mainly defined by an uncertainty in the calibration of 80 K, as given by Mucciarelli et al. (2021).

To estimate our initial surface gravities ($\log g$), we made use of distances based on *Gaia* parallaxes and isochrones. Parallaxes are corrected for the zero offset according to Lindegren et al. (2021) and distances are computed from the maximum of the probability distribution function as described in Bailer-Jones (2015). With these distances, effective temperatures, bolometric

² <https://www.eso.org/sci/software/pipelines/>

³ <https://astroutils.astronomy.osu.edu/exofast/barycorr.html>

⁴ IRAF is distributed by the National Optical Astronomy Observatory, which is operated by the Association of Universities for Research in Astronomy (AURA) under a cooperative agreement with the National Science Foundation.

⁵ <http://www.subarutelescope.org/Observing/Instruments/HDS/hdsq1-e.html>

Table 1. Stellar sample, stellar parameters, and characteristics of the observed spectra.

<i>Gaia</i> ID	RA deg.	Dec deg.	G mag.	E(B-V) mag.	S/T ⁽¹⁾	t_{exp} , min.	S/N _B	S/N _R	T_{eff} , K	log g cm s ⁻²	[Fe/H]	ξ_t , km s ⁻¹	d_{spec} , kpc	v_r , km s ⁻¹
Cetus-New														
2483903595868274048	23.194442	-3.811474	13.99	0.032	U	30	29	46	4440	0.94	-2.10 ± 0.05	1.7	18.2 ± 2.8	43.5
2795091499930032768	10.415858	-18.780757	14.28	0.045	H	30	20	53	4400	0.70	-2.53 ± 0.15	1.8	26.3 ± 4.0	-83.5
2479610243479857792	24.259206	-5.924668	14.41	0.035	U	30	26	41	4560	1.20	-1.99 ± 0.08	1.7	17.6 ± 2.6	58.0
2512532782711324288	27.890108	3.048892	14.91	0.027	H	30	24	77	4625	1.30	-1.98 ± 0.06	1.7	20.8 ± 3.1	44.5
320073130541422080	19.339750	33.959461	15.20	0.040	H	30	14	21	4620	1.00	-2.20 ± 0.11	2.1	32.8 ± 4.9	-65.5
2505061738639700608	29.090208	-1.975403	15.22	0.024	M	25	37	53	4930	1.85	-1.85 ± 0.10	1.8	15.0 ± 2.2	53.5
					H	30	27	62						
5036037656380706560	23.899406	-26.841977	15.23	0.012	M	30	32	35	4905	1.90	-1.50 ± 0.08	1.9	14.3 ± 2.1	81.9
392208686827199744	3.583298	46.930416	15.24	0.093	H	30	15	53	4540	1.10	-2.10 ± 0.11	1.9	26.8 ± 4.0	-113.5
291112234783352320	26.944332	24.114584	15.29	0.102	H	30	12	42	4285	0.71	-1.94 ± 0.14	1.9	36.2 ± 5.5	-46.5
5008704278351937280	23.906688	-38.859709	15.67	0.011	M	50	39	51	4940	1.92	-2.04 ± 0.13	1.5	17.4 ± 2.6	54.5
Cetus-Palca														
1918128584760819968	349.622498	39.983749	14.25	0.109	H	30	19	70	4420	0.85	-2.18 ± 0.11	1.8	20.6 ± 3.1	315.0
2454009833214133376	25.256498	-13.688868	14.70	0.016	M	30	36	52	4600	1.20	-1.99 ± 0.09	1.9	21.1 ± 3.2	-144.1
299322872223728000	27.626137	28.865772	14.73	0.052	H	30	25	44	4500	1.00	-2.12 ± 0.09	1.7	24.3 ± 3.7	209.0
110194640179380864	44.152267	23.833143	14.84	0.158	H	20	15	43	4610	1.19	-2.22 ± 0.08	1.7	19.5 ± 2.9	-152.0
137407896564837376	48.409805	33.542347	14.91	0.165	H	30	18	59	4325	0.65	-2.17 ± 0.11	1.7	31.0 ± 4.7	161.0
2457328468544765184	24.417424	-12.552211	14.97	0.018	M	30	32	46	4545	0.98	-2.04 ± 0.09	1.8	29.8 ± 4.5	-81.9
2507540140928136832	30.152781	-0.309415	15.10	0.024	H	30	15	53	4500	0.95	-2.35 ± 0.06	1.8	31.4 ± 4.7	-68.0
2532901132536856320	18.053215	-1.234548	15.15	0.053	M	30	29	51	4455	0.96	-1.90 ± 0.17	1.8	30.0 ± 4.5	-106.3
2502895425855079424	37.896091	1.442148	15.41	0.023	M	25	28	37	4685	1.33	-2.48 ± 0.06	1.7	26.2 ± 3.9	-109.4
2818454438393552256	347.123444	16.893238	15.42	0.126	H	30	14	48	4650	1.34	-2.09 ± 0.12	1.9	22.7 ± 3.4	-244.0
5012153068370401664	26.448789	-33.961611	15.56	0.021	M	50	40	49	4790	1.54	-2.32 ± 0.11	1.6	23.4 ± 3.5	-81.2
2450913123138677376	23.160807	-16.835150	15.85	0.018	M	50	33	53	4675	1.32	-2.21 ± 0.13	2.0	32.5 ± 4.8	4.7

Notes. ⁽¹⁾ Spectrograph/Telescope: U – UVES/VLT, M – MIKE/Magellan, H – HDS/Subaru.

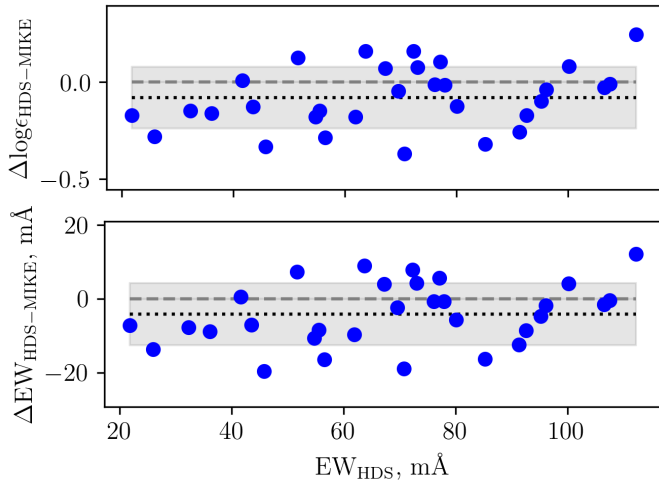


Fig. 2. Abundance difference between iron lines measured in *Gaia* DR3 2505061738639700608 spectra taken with the HDS and MIKE instruments (top panel) and the corresponding abundance differences in EWs (bottom panel) as a function of EW. The dotted lines and shaded areas in both panels represent the mean difference and 1 σ dispersion.

corrections of Casagrande & Vandenberg (2018), and assuming a mass of 0.8 solar masses, we derive surface gravities using the formula $\log g = 4.44 + \log(m/m_{\odot}) + 0.4(M_{\text{bol}} - 4.75) + 4 \log(T_{\text{eff}}/5780)$, where m_{\odot} is a solar mass and M_{bol} is an absolute bolometric magnitude. For our sample stars, the ratio

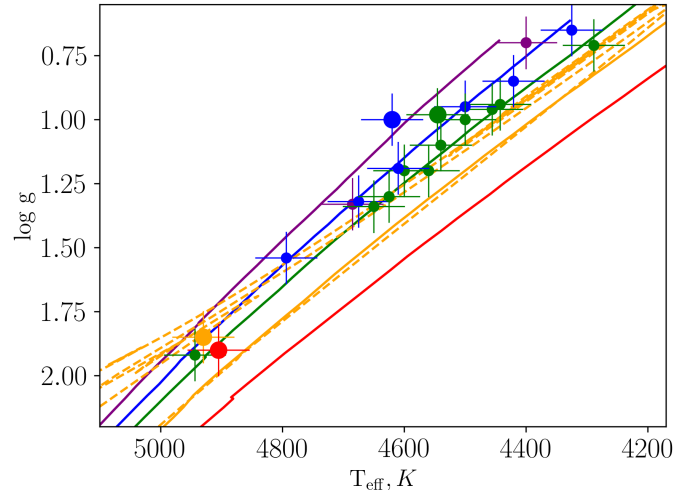


Fig. 3. Positions of the sample stars on giant branches of 12 Gyr isochrones (Dotter et al. 2008, solid lines) with [Fe/H] from -2.5 (violet) to -1.5 (red) with a step of 0.25 dex. For comparison, we show the 12 Gyr Dotter (2016) isochrone with [Fe/H] = -1.75, which includes advanced evolutionary stages (dashed orange line). Larger symbols represent stars at more advanced evolutionary stages. The symbols have the same metallicity colour coding as the lines.

between the parallax error and the parallax exceeds 0.2 and the uncertainty in distance results in an uncomfortably large

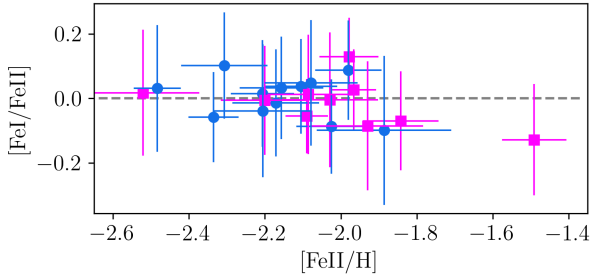


Fig. 4. NLTE abundance difference between Fe I and Fe II as a function of metallicity $[\text{Fe II}/\text{H}]$. The Cetus-New stars and the Cetus-Palca stars are shown with magenta squares and blue circles, respectively.

uncertainty of 0.3 dex in $\log g$. Consequently, we refine the initially calculated $\log g$ values using the 12 Gyr isochrones with $[\text{Fe}/\text{H}] = -2$ and $[\alpha/\text{Fe}] = 0.4$ (Dotter et al. 2008), as described below.

Starting with the first step parameters, we calculated NLTE abundances using Fe I and Fe II lines. To further refine the stellar parameters, we used the difference in NLTE abundance from Fe I and Fe II, along with the derived $[\text{Fe}/\text{H}]$. This refinement process involves fitting isochrones with $[\text{Fe}/\text{H}]$ values ranging from -2.5 to -1.5 , and is designed to keep abundances from the Fe I and Fe II lines consistent within the error bars. It is worth noting that using the same method for iron NLTE abundance determination, Mashonkina et al. (2017a) found consistent Fe I and Fe II abundances in VMP giants with photometric effective temperatures and accurate distance-based surface gravities.

The tuning procedure is repeated until a reasonable convergence between isochrones, ionisation balance, and metallicity is achieved. When a given star's parameters (T_{eff} , $\log g$, and $[\text{Fe}/\text{H}]$) are found to be within 50 K and 0.1 dex of the corresponding isochrone, and the NLTE abundances from Fe I and Fe II lines agree within the error bars, we adopt these parameters as the final values. Based on the criteria mentioned above, we assign uncertainties of 50 K for T_{eff} and 0.1 dex for $\log g$. Figure 4 shows the NLTE abundance difference between Fe I and Fe II as a function of metallicity based on the Fe II lines. The difference never exceeds 0.13 dex in absolute value and, for the 22 sample stars, the average NLTE difference amounts to $\text{Fe I} - \text{Fe II} = -0.01 \pm 0.07$. The microturbulent velocity is derived from the lines of Fe I and Fe II and its uncertainty amounts to 0.2 km s^{-1} .

Among the sample stars, four do not align with the giant branch with the corresponding $[\text{Fe}/\text{H}]$ and their positions are shifted towards higher T_{eff} and/or lower $\log g$. Changing T_{eff} and $\log g$ leads to a discrepancy between abundances from Fe I and Fe II. These stars might be at more advanced evolutionary stages than the red giant branch, such as early asymptotic giant branch (AGB) stars in a phase prior to the onset of thermal pulses. The Dotter (2016) isochrone, which accounts for advanced evolutionary stages, supports this guess (see Fig. 3).

With our final surface gravities, we calculate the corresponding distances, referred to as spectroscopic distances (d_{spec}). These are listed in Table 1. The distances to our sample stars range from 14 to 36 kpc. These results can be employed for improving the precision of the orbits and characteristics of the Cetus stream's progenitor. It is worth noting that our distances differ significantly from those provided by the *Gaia* DR3 catalogue (Gaia Collaboration 2021, distances from GSP-Phot Aeneas best library using BP/RP spectra) and the Bailer-Jones et al. (2021) catalogue, which provide unexpectedly small values for our sample stars from 2.3 to 8.5 kpc and from 5.2 to 12.4 kpc, respectively.

4. Abundance analysis methods

4.1. Codes and model atmospheres

We use classical 1D model atmospheres from the MARCS model grid (Gustafsson et al. 2008), interpolated for the given T_{eff} , $\log g$, and $[\text{Fe}/\text{H}]$ of the stars. We solve the coupled radiative transfer and statistical equilibrium equations with the DETAIL code (Giddings 1981; Butler 1984) using the updated opacity package as presented by Mashonkina et al. (2011). For synthetic spectra calculations, we use the SYNTHV_NLTE code (Tsybal et al. 2019) attached to the IDL BINMAG code (Kochukhov 2018). This technique allows us to obtain the best fit to the observed line profiles with the NLTE effects taken into account via pre-calculated departure coefficients (the ratio between NLTE and LTE atomic level populations) for a given model atmosphere. When fitting the line profiles, the abundance of the element of interest is varied together with the macroturbulent velocity (v_{mac}) and the radial velocity (v_r).

The line list for spectral synthesis is extracted from a recent version of the Vienna Atomic Line Database (VALD, Pakhomov et al. 2019; Ryabchikova et al. 2015), which provides isotopic and hyperfine structure components of the spectral lines for a number of studied chemical elements. We adopt the oscillator strengths recommended by VALD. The exception is Fe II, where we take gf -values from Raassen & Uylings (1998) corrected by +0.11 dex, following the recommendation of Grevesse & Sauval (1999). The same approach was adopted in the earlier studies of VMP stars (Mashonkina et al. 2017a,b, 2019a). For barium, we determine abundances using two different isotope ratios – solar mixture, as provided by VALD by default, and the r -process ratio taken from Arlandini et al. (1999). For the Ba II resonance line at 4554 Å, using the r -process ratio leads to lower abundances compared to those derived with the solar mixture, and the abundance shifts vary from 0.06 dex to 0.20 dex in our sample stars with EW_{4554} from 280 to 140 mÅ, respectively. The subordinate lines of Ba II are weaker and their abundances are nearly immune to the adopted isotope ratio. Our average barium abundances rely only on the subordinate Ba II lines. For each star, we provide abundances from individual spectral lines together with their atomic data and measured EWs; see Table 2.

4.2. NLTE effects

We take into account the departure from LTE for a number of species: O I (Sitnova & Mashonkina 2018), Na I (Alexeeva et al. 2014), Mg I (Mashonkina 2013), Al I (Lind et al. 2022), S I (Takeda et al. 2005), K I (Neretina et al. 2020), Ca I (Mashonkina et al. 2017c), Sc II (Mashonkina & Romanovskaya 2022), Ti II (Sitnova et al. 2020), Cr I (Bergemann & Cescutti 2010), Mn I (Bergemann et al. 2019), Fe I (Mashonkina et al. 2011), Co I (Bergemann et al. 2010), Cu I (Caffau et al. 2023), Zn I (Sitnova et al. 2022), Sr II (Mashonkina et al. 2022; Yakovleva et al. 2022), Y II (Alexeeva et al. 2023), Zr II (Velichko et al. 2010), Ba II (Mashonkina & Belyaev 2019), and Eu II (Mashonkina & Gehren 2000). We refer the reader to the papers listed above for the description of the model atoms and the mechanism of the NLTE effects. For those interested in the original NLTE studies conducted from the 1960s to the present, we suggest the bibliography compiled by Sitnova et al. (2018) and available on the web page <https://non-lte.com/bibliography.html>.

For species where NLTE effects are taken into account, we present the differences between the average NLTE and LTE abundances in our Cetus stars as a function of metallicity

Table 2. NLTE and LTE abundances from individual lines and their atomic data.

<i>Gaia</i> ID	Sp.	λ , Å	E_{exc} , eV	log gf	EW, mÅ	log ϵ LTE	log ϵ NLTE
2483...	CH	4192.56	0.64	-1.28	19.0	5.37	
2483...	CH	4210.94	0.46	-1.34	24.4	5.29	
2483...	O I	6300.30	0.00	-9.78	24.1	7.25	7.25
2483...	Na I	5889.95	0.00	0.11	249.1	4.05	3.86
2483...	Na I	5895.92	0.00	-0.19	222.2	4.05	3.81
2483...	Na I	8183.25	2.10	0.24	63.3	3.99	3.90
2483...	Na I	8194.80	2.10	0.49	87.4	3.99	3.85
2483...	Mg I	4702.99	4.35	-0.44	116.2	5.76	5.71
2483...	Mg I	5711.09	4.35	-1.72	41.4	5.78	5.76
2483...	Al I	3961.52	0.01	-0.32	186.0	3.95	4.05
2483...	Si I	4102.94	1.91	-3.14	120.7	5.86	
2483...	Si I	5948.54	5.08	-1.23	25.1	5.84	
2483...	Si I	6155.13	5.62	-0.76	12.5	5.65	
2483...	Si I	7932.35	5.96	-0.47	11.7	5.68	
2483...	S I	9212.86	6.52	0.47	43.5	5.40	5.17
2483...	K I	7698.96	0.00	-0.15	108.2	3.39	3.01
2483...	Ca I	5857.45	2.93	0.23	70.6	4.49	4.55
2483...	Ca I	6102.72	1.88	-0.79	91.2	4.45	4.52
2483...	Ca I	6122.22	1.89	-0.31	124.8	4.54	4.57
2483...	Ca I	6169.04	2.52	-0.80	45.6	4.57	4.73
2483...	Ca I	6439.07	2.53	0.39	108.6	4.40	4.34
2483...	Ca I	6471.66	2.53	-0.69	44.9	4.43	4.50
2483...	Ca I	6493.78	2.52	-0.11	73.8	4.30	4.32
2483...	Ca I	6499.65	2.52	-0.82	32.5	4.34	4.43
2483...	Sc II	4400.38	0.61	-0.54	107.8	1.01	0.98
2483...	Sc II	4415.54	0.60	-0.68	111.5	1.16	1.15
2483...	Sc II	6245.64	1.51	-1.02	35.1	1.03	1.05
2483...	Ti I	4840.87	0.90	-0.43	52.6		
2483...	Ti I	4913.61	1.87	0.16	14.3		
2483...	Ti I	4981.73	0.85	0.57	100.2		
2483...	Ti I	6261.10	1.43	-0.53	22.0		
2483...	Ti II	4764.52	1.24	-2.69	51.5	3.18	3.18
2483...	Ti II	4798.53	1.08	-2.66	73.3	3.35	3.35
2483...	Ti II	4911.19	3.12	-0.64	21.1	2.85	2.85
2483...	Ti II	6491.57	2.06	-1.94	35.8	3.07	3.07

Notes. The table is accessible in a machine-readable format at the CDS. A portion is shown to illustrate its format and content.

(Fig. 5). For oxygen, our abundance determinations mostly rely on the O I 6300 Å line, where NLTE effects are negligible; hence, we do not show the corresponding differences. In the most metal-rich star of our sample, we also use the O I 7771 Å line and apply a NLTE abundance correction of -0.20 dex. Abundances of sodium and aluminium are strongly affected by NLTE effects. For sodium, the difference between NLTE and LTE abundances reaches down to -0.6 dex. For the Al I 3961 Å line, NLTE corrections are positive and they take values of up to 0.2 dex. For magnesium and calcium, NLTE effects are small and they result in up to 0.1 dex lower and higher abundances, respectively. Accounting for the NLTE effects is particularly essential for S I and K I, where NLTE typically yields 0.4 dex lower abundances compared to LTE. Sc II and Ti II are the majority species in the investigated stellar parameter range and NLTE leads to a moderate positive shift in their abundances of up to 0.1 dex. NLTE corrections are positive for lines of neutral species of the iron-group elements and copper. However, the magnitudes of the

NLTE effects are different for different elements, with a typical shift between NLTE and LTE abundances of 0.1 dex for Fe I and of as much as 1 dex for Co I. Abundances of n-capture elements are derived from lines of the singly ionised atoms, which are all the majority species in the atmospheres of the sample stars. The NLTE effects for these lines are moderate and they result in an abundance difference of up to 0.2 dex in absolute value.

For most chemical elements, we perform NLTE calculations with the specific model atmospheres, while for Al I, Cr I, Mn I, Co I, and Zn I, we interpolate the NLTE abundance corrections in the precalculated grids available in the literature. It is worth noting that a reasonable amount of data has been accumulated on the NLTE abundance corrections for different species, and these can be retrieved from the following user-friendly databases: https://nlte.mpia.de/gui-siuAC_secEnew.php (M. Kovalev and M. Bergemann), inspect-stars.com (K. Lind), and <http://spectrum.inasan.ru/nLTE2/> (Mashonkina et al. 2023). Abundances of C, Si, V, Ni, La, Ce, Nd, Sm, and Dy are determined under the LTE assumption.

Our carbon abundance is based on the LTE analysis of the molecular CH lines. Popa et al. (2023) report notable NLTE effects for the CH lines, with positive NLTE corrections that grow with decreasing metallicity. These authors calculate $\Delta_{\text{NLTE}} = 0.15$ dex for the model 4500/2.0/ -2.0 with $[C/Fe] = 0.0$. At the same time, Alexeeva & Mashonkina (2015) found the LTE abundance from the CH lines to be consistent with the NLTE abundance from the C I lines for cool stars with well-determined stellar atmosphere parameters.

For Si I, NLTE effects are minor and can be neglected even in metal-poor stars (Mashonkina et al. 2016). For V I–II NLTE calculations are not available in the literature. For our sample of stars, where both V I and V II lines are detected, we find a systematically lower LTE abundance from V I compared to V II, and the difference spans from -0.3 to -0.7 dex. This result can be explained by the fact that V I is the least abundant species and may suffer from overionisation, which leads to positive NLTE abundance corrections, while V II is the most abundant species in the investigated atmosphere parameter range and minor NLTE abundance corrections are expected.

The departures from LTE for Ni I in the solar atmosphere were investigated by Bruls (1993), Vieytes & Fontenla (2013), Bergemann et al. (2021), and Magg et al. (2022) and in FGK stars by Eitner et al. (2023). For Ni I lines in the visible range, Eitner et al. (2023) predict positive NLTE abundance corrections, increasing towards higher T_{eff} and lower log g. For example, these latter authors found $\Delta_{\text{NLTE}} \sim 0.2$ dex in the model atmosphere with $T_{\text{eff}}/\log g/[Fe/H] = 5000/3/-2.5$.

We plan to study the NLTE calculations for La II, Ce II, Nd II, Sm II, and Dy II in late-type stars. The above species form the majority of the species found in atmospheres of cool stars, and one might expect moderate or minor NLTE effects.

5. Comparison samples: MW halo and UMi dSph

For the purpose of comparison, we adopted a sample of the MW halo stars and a sample of stars from the UMi dSph that were analysed using similar methods to those of this study. The choice of the UMi dSph is motivated by its stellar mass of $M_* = 10^{5.5} M_{\odot}$ (McConnachie 2012), $10^{5.7} M_{\odot}$ (Kirby et al. 2013), which is similar to the progenitor mass of the Cetus stream $M_* = 10^{5.6} M_{\odot}$ (Yuan et al. 2022). Another reason is that the UMi dSph is one of the most well-studied nearby dwarf galaxies. High-resolution optical spectra were obtained for more than

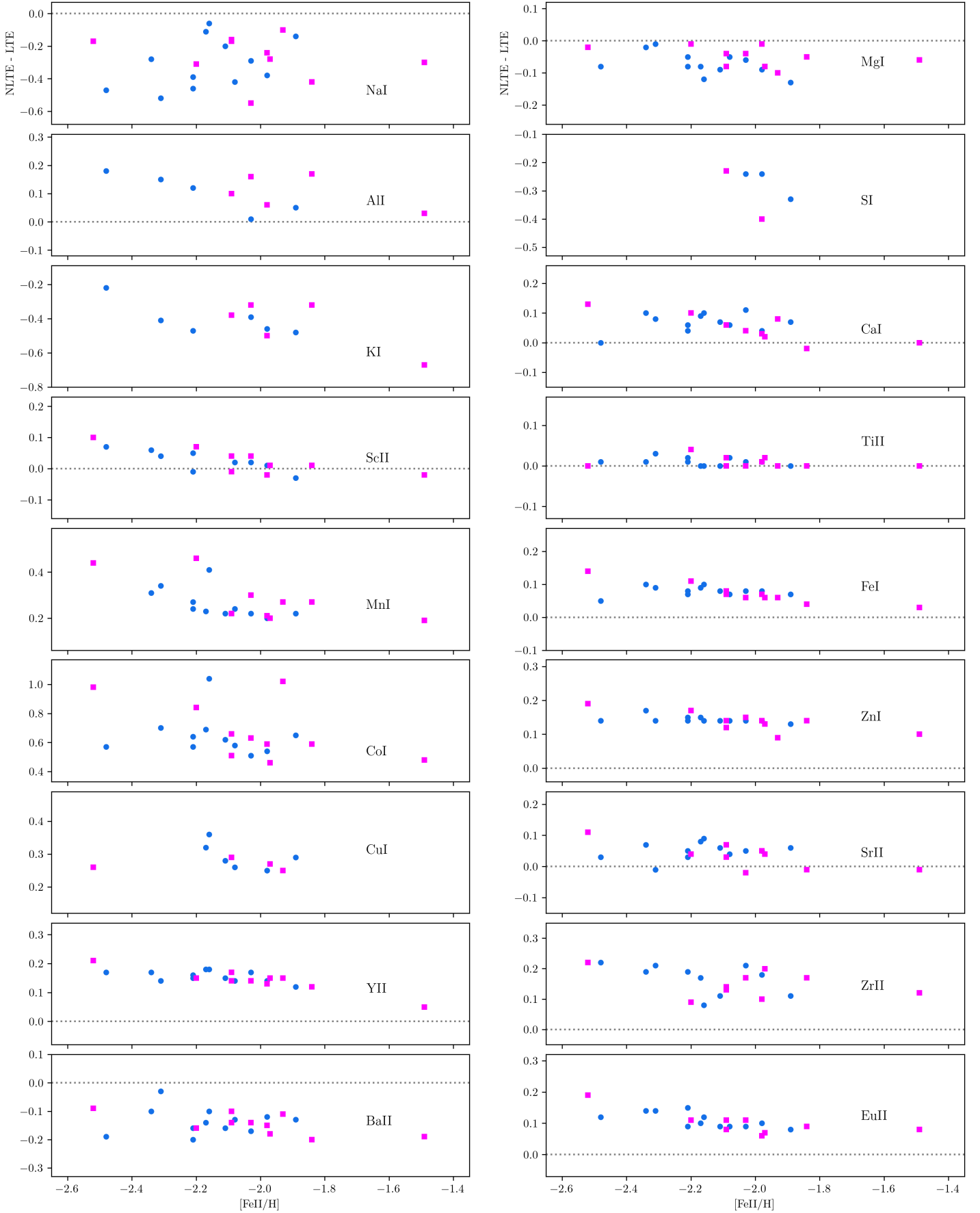


Fig. 5. Differences between the NLTE and LTE average abundance of different chemical species in the Cetus-New (magenta squares) and Cetus-Palca (blue circles) sample stars plotted as a function of metallicity.

a dozen UMi stars (Shetrone et al. 2001; Sadakane et al. 2004; Aoki et al. 2007b; Cohen & Huang 2010; Ural et al. 2015; Kirby & Cohen 2012; Sestito et al. 2023). These latter analysis yielded valuable insights into the chemical evolution history of the UMi dSph. In this study, we do not aim to reinvestigate the UMi chemical evolution and we simply use its stellar abundances for comparison with those derived in the Cetus stars. For consistency, we reanalyse abundances for some of the UMi stars with the methods adopted in this study.

5.1. MW halo stars

Our MW halo comparison sample includes VMP dwarfs and giants. For dwarfs, photometric effective temperatures and distance-based surface gravities were determined by Sitnova et al. (2015). For each star, NLTE abundances of Fe I and Fe II were obtained that are consistent within the error bars. For the MW halo giants, surface gravities were determined from NLTE abundances of Fe I and Fe II (Mashonkina et al. 2017a, hereafter MJ17a). These gravities were confirmed by calculations of Mashonkina et al. (2023) based on accurate *Gaia* parallaxes.

For the dwarfs, the NLTE abundances for a number of species are taken from Zhao et al. (2016). In addition, we employ previously determined NLTE abundances of scandium (Mashonkina & Romanovskaya 2022), zinc (Sitnova et al. 2022), and yttrium (Alexeeva et al. 2023) for our star sample. For the giants, the NLTE abundances are taken from Mashonkina et al. (2017b, hereafter MJ17b). For oxygen, potassium, scandium, chromium, manganese, cobalt, copper, and zinc, MJ17b do not present abundances and so we adopted those of Sitnova et al. (in prep.). The same line lists and NLTE methods used for the Cetus stars (see Sect. 4) were applied to determine the abundances in the MW halo stars.

5.2. UMi dSph

We adopt the NLTE abundances of the UMi dSph VMP stars from MJ17b, which are based on the high-resolution spectra collected by Cohen & Huang (2010, hereafter CH10), Kirby & Cohen (2012), and Ural et al. (2015). The studies of MJ17a and MJ17b focus on the early chemical enrichment and are therefore limited to stars with $[\text{Fe}/\text{H}] < -2$. Fortunately, CH10 provide EWs for the UMi stars in the metal-poor regime ($-1 > [\text{Fe}/\text{H}] > -2$) based on their high-resolution spectra. Here, we supplement the UMi sample from MJ17b by including four UMi stars from CH10 and redetermine their abundances using our linelist and considering NLTE effects. In addition, we include a VMP UMi star recently discovered by Sestito et al. (2023, hereafter, SZ23). For consistency, we reanalysed this star using our methods.

For the four metal-poor stars, namely COS171, JI2, N37, and 27940, we take the photometric T_{eff} and distance-based $\log g$ from CH10. Stellar parameters of CH10 rely on $V - I$, $V - J$, and $V - H$ colours, isochrones, distances, and analyses of the spectra. For comparison, we calculated T_{eff} and $\log g$ for COS171 using *Gaia* photometry, $E(B-V) = 0.028$, a distance of 69 kpc (Mighell & Burke 1999), the bolometric corrections from Casagrande & Vandenberg (2018), $[\text{Fe}/\text{H}] = -1.3$, and $m = 0.8m_{\odot}$. We find $T_{\text{eff}} = 4315 \pm 80$ K and $\log g = 0.84 \pm 0.06$, which are consistent within the error bars with $T_{\text{eff}} = 4380$ K and $\log g = 0.80$, as recommended by CH10. For the VMP star from SZ23, we find T_{eff} , $\log g$, $[\text{Fe}/\text{H}]$, and ξ_t of 4615 ± 85 K, 1.24 ± 0.06 , -2.01 ± 0.17 , and $1.8 \pm 0.2 \text{ km s}^{-1}$, respectively, which are consistent within the error bars with the values found by SZ23.

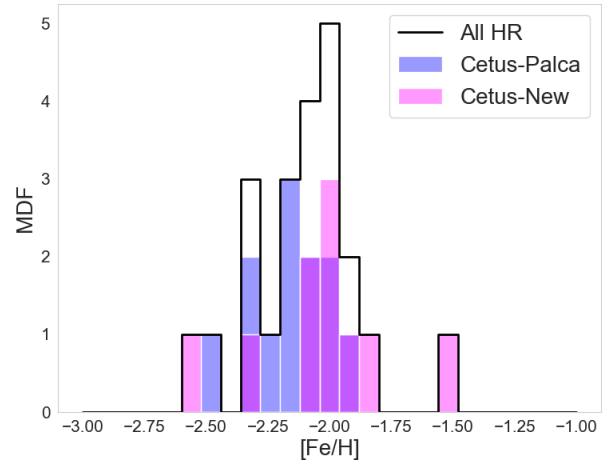


Fig. 6. Metallicity distribution function of all 22 Cetus stars in the HR follow up gives a mean $[\text{Fe}/\text{H}] = -2.11$ with an intrinsic dispersion of 0.21 dex (black histogram). The MDFs of the Cetus-Palca (blue histogram) and Cetus-New (magenta histogram) wraps almost overlap.

For the four CH10 stars, we employ the EWs provided in the original study and our linelist to determine their abundances, while for SZ23 star, we use the observed spectrum. We note that the barium abundances of UMi stars rely only on the subordinate lines, which are not affected by the adopted barium odd/even isotope ratio. The NLTE and LTE abundance ratios are presented in Table 3, along with the stellar parameters for the five metal-poor UMi stars. It is worth noting that the UMi sample contains a peculiar star, COS171, which is enhanced in iron, and thus shows low $[\text{X}/\text{Fe}]$ ratios; for example, $[\text{Mg}/\text{Fe}] = -0.63 \pm 0.13$. Similar iron-rich stars are known in the literature, such as the star ET0381 discovered by Jablonka et al. (2015) in the Sculptor dSph and the three MW halo stars identified by Reggiani et al. (2023).

6. Results

6.1. Metallicity distribution function

Using the derived metallicities, we confirm that the two Cetus wraps have similar metallicity distribution functions (MDFs). They are shown in Fig. 6. By taking into account the uncertainty in $[\text{Fe}/\text{H}]$ for each star, the mean metallicity in the Cetus-Palca is -2.19 with an intrinsic dispersion of 0.12 dex. The Cetus-New wrap has a mean metallicity of -2.02 , and a larger dispersion of 0.25 dex. The total sample of 22 Cetus stars gives a mean $[\text{Fe}/\text{H}] = -2.11 \pm 0.21$, consistent with the previous findings: $[\text{Fe}/\text{H}] = -2.07 \pm 0.12$ from LAMOST K giants in Liu et al. (2014) and Yuan et al. (2019); and $[\text{Fe}/\text{H}] = -2.17$ (Yuan et al. 2022) from 35 member stars with photometric metallicities based on Pristine survey (Starkenburg et al. 2017) and SkyMapper DR2 (Huang et al. 2022).

Using the two-sample Kolmogorov-Smirnov test, we examined whether the samples from Cetus-New and Cetus-Palca originate from the same distribution. We find a resulting probability p -value = 14%, indicating a 14% chance of rejecting our hypothesis that the two samples come from the same distribution. The metallicity dispersion of 0.21 dex confirms that the Cetus progenitor was a dwarf galaxy rather than a globular cluster. Globular clusters exhibit a narrower metallicity dispersion, typically less than 0.05 dex (see e.g. Li et al. 2022).

Table 3. Stellar parameters and abundance ratios of the UMi dSph stars.

Sp.	$\log \varepsilon_{\odot}^{(*)}$	[X/H]	[X/Fe II]	[X/H]	[X/Fe II]	N
		LTE	LTE	NLTE	NLTE	
UMi COS171: 4380 / 0.80 / -1.28 / 1.8						
Na I	6.27	-2.74 ± 0.13	-1.47	-2.77 ± 0.16	-1.50	3
Mg I	7.52	-1.84 ± 0.16	-0.57	-1.89 ± 0.13	-0.62	3
Ca I	6.27	-1.63 ± 0.09	-0.36	-1.49 ± 0.11	-0.23	4
Ti II	4.90	-1.70 ± 0.06	-0.43	-1.70 ± 0.06	-0.43	5
Cr I	5.63	-2.07 ± 0.11	-0.84	-1.95 ± 0.07	-0.72	3
Fe I	7.45	-1.50 ± 0.08	-0.24	-1.46 ± 0.07	-0.20	20
Fe II	7.45	-1.27 ± 0.05	0.00	-1.27 ± 0.05	0.00	4
Ni I	6.20	-1.95	-0.68			1
Zn I	4.61	-2.45 ± 0.04	-1.18	-2.33 ± 0.05	-1.06	2
Sr II	2.88	-1.86	-0.59	-1.83	-0.56	1
Ba II	2.17	-2.11 ± 0.14	-0.84	-2.17 ± 0.14	-0.91	3
Eu II	0.51	-1.42	-0.15	-1.35	-0.08	1
UMi J12: 4415 / 0.85 / -1.76 / 1.9						
Na I	6.27	-2.46 ± 0.07	-0.71	-2.55 ± 0.14	-0.80	4
Mg I	7.52	-1.69 ± 0.11	0.06	-1.76 ± 0.07	-0.01	3
Ca I	6.27	-1.69 ± 0.02	0.07	-1.59 ± 0.04	0.16	4
Ti II	4.90	-1.59 ± 0.13	0.17	-1.59 ± 0.13	0.17	4
Cr I	5.63	-2.11 ± 0.06	-0.40	-1.99 ± 0.08	-0.28	2
Fe I	7.45	-1.90 ± 0.08	-0.15	-1.84 ± 0.08	-0.09	25
Fe II	7.45	-1.75 ± 0.10	0.00	-1.75 ± 0.10	0.00	3
Ni I	6.20	-1.91	-0.16			1
Zn I	4.61	-2.14 ± 0.06	-0.38	-2.03 ± 0.07	-0.28	2
Ba II	2.17	-1.44 ± 0.09	0.31	-1.56 ± 0.08	0.19	3
Eu II	0.51	-0.85 ± 0.05	0.90	-0.81 ± 0.04	0.95	2
UMi N37: 4390 / 0.80 -1.55 / 1.8						
Na I	6.27	-2.29 ± 0.09	-0.65	-2.35 ± 0.14	-0.71	4
Mg I	7.52	-1.54 ± 0.10	0.10	-1.61 ± 0.04	0.03	3
Ca I	6.27	-1.51 ± 0.08	0.13	-1.41 ± 0.11	0.23	4
Ti II	4.90	-1.46 ± 0.03	0.18	-1.46 ± 0.03	0.18	4
Cr I	5.63	-1.93 ± 0.05	-0.33	-1.77 ± 0.13	-0.17	3
Fe I	7.45	-1.67 ± 0.09	-0.03	-1.61 ± 0.09	0.03	21
Fe II	7.45	-1.64 ± 0.09	0.00	-1.64 ± 0.09	0.00	5
Ni I	6.20	-1.65	-0.01			1
Zn I	4.61	-2.05 ± 0.02	-0.41	-1.98 ± 0.01	-0.33	2
Ba II	2.17	-1.35 ± 0.03	0.29	-1.45 ± 0.01	0.19	3
Eu II	0.51	-0.69 ± 0.08	0.95	-0.65 ± 0.07	1.00	2
UMi 27940: 4290 / 0.70 / -1.77 / 1.9						
Na I	6.27	-2.32 ± 0.14	-0.56	-2.35 ± 0.13	-0.59	4
Mg I	7.52	-1.70 ± 0.12	0.07	-1.78 ± 0.05	-0.02	3
Ca I	6.27	-1.77 ± 0.03	-0.01	-1.69 ± 0.05	0.08	3
Ti II	4.90	-1.73 ± 0.06	0.03	-1.73 ± 0.06	0.03	4
Cr I	5.63	-2.28 ± 0.11	-0.56	-2.05 ± 0.05	-0.33	3
Fe I	7.45	-2.03 ± 0.09	-0.26	-1.98 ± 0.09	-0.21	23
Fe II	7.45	-1.76 ± 0.18	0.00	-1.76 ± 0.18	0.00	4
Ni I	6.20	-2.08	-0.32			1
Zn I	4.61	-2.24 ± 0.02	-0.47	-2.13 ± 0.02	-0.37	2
Sr II	2.88	-2.19	-0.43	-2.13	-0.37	1
Ba II	2.17	-1.82 ± 0.16	-0.06	-1.91 ± 0.18	-0.15	3
Eu II	0.51	-1.40 ± 0.01	0.36	-1.31 ± 0.00	0.45	2
UMi T1SZ23: 4615 / 1.24 / -2.01 / 1.8						
Na I	6.27	-2.57 ± 0.02	-0.56	-2.83 ± 0.12	-0.82	3
Mg I	7.52	-1.21 ± 0.10	0.80	-1.33 ± 0.18	0.68	2
Si I	7.51	-1.68 ± 0.21	0.33	-1.68 ± 0.21	0.33	4
K I	5.07	-1.99	0.02	-2.20	-0.19	1
Ca I	6.27	-1.79 ± 0.16	0.22	-1.77 ± 0.20	0.24	9
Sc II	3.04	-1.94 ± 0.12	0.07	-1.93 ± 0.12	0.08	3
Ti II	4.90	-1.89	0.12	-1.89	0.12	1
Cr I	5.63	-2.34 ± 0.30	-0.33	-2.06 ± 0.29	-0.05	4
Fe I	7.45	-2.07 ± 0.22	-0.06	-2.00 ± 0.22	0.01	45
Fe II	7.45	-2.01 ± 0.16	0.00	-2.01 ± 0.16	0.00	8
Ni I	6.20	-2.17 ± 0.11	-0.16			5
Ba II	2.17	-2.90 ± 0.09	-0.88	-2.90 ± 0.10	-0.89	2

Notes. ^(*)Solar abundances are taken from [Lodders \(2021\)](#).

Table 4. NLTE and LTE abundance ratios of the Cetus stars.

Gaia ID	Sp.	[X/H]	[X/Fe II]	[X/H]	[X/Fe II]	N
		LTE	LTE	NLTE	NLTE	
2483...	CH	-3.14 ± 0.04	-1.05			2
2483...	O I	-1.48	0.61	-1.48	0.61	1
2483...	Na I	-2.25 ± 0.03	-0.16	-2.41 ± 0.03	-0.32	4
2483...	Mg I	-1.75 ± 0.01	0.34	-1.79 ± 0.02	0.31	2
2483...	Al I	-2.47	-0.38	-2.37	-0.28	1
2483...	Si I	-1.75 ± 0.09	0.34			4
2483...	S I	-1.75	0.34	-1.98	0.11	1
2483...	K I	-1.68	0.41	-2.06	0.03	1
2483...	Ca I	-1.83 ± 0.09	0.26	-1.77 ± 0.12	0.32	8
2483...	Sc II	-1.97 ± 0.07	0.12	-1.98 ± 0.07	0.11	3
2483...	Ti II	-1.79 ± 0.18	0.30	-1.79 ± 0.18	0.30	4
2483...	V I	-2.65 ± 0.01	-0.56			2

Notes. The table is accessible in a machine-readable format at the CDS. A portion is shown to illustrate its format and content.

6.2. Abundance trends

Table 4 presents the LTE and NLTE abundances together with their statistical uncertainties and the number of lines used. The abundance uncertainty is calculated as the dispersion of the single line measurements around the mean $\sigma = \sqrt{\Sigma(\log \varepsilon - \log \varepsilon_i)^2 / (N - 1)}$, where N is the total number of lines. The abundance trends are presented in Figs. 7–16. For our sample stars and for the comparison samples, we calculated abundance ratios using solar abundances from [Lodders \(2021\)](#).

6.2.1. Carbon

Our sample stars exhibit a depleted carbon abundance with respect to iron, and [C/Fe] spans from -1.2 to -0.2 depending on stellar luminosity (Fig. 7). The sample stars are giants and therefore suffer from carbon depletion caused by the dredge up. According to the classification suggested by [Aoki et al. \(2007a\)](#), the Cetus stars belong to the carbon-normal population.

Our analysis reveals that none of the Cetus stars with measured carbon abundance exhibit carbon enhancement, which is noteworthy given that carbon-enhanced stars with [C/Fe] > 0.7 (CE, [Aoki et al. 2007a](#)) are numerous among VMP stars ([Placco et al. 2014](#); [Ji et al. 2020b](#)). Our result aligns with the significantly lower fraction of CE metal-poor (CEMP) stars in dSph galaxies compared to that in the MW and UFDs found by [Lucchesi et al. \(2024\)](#). In the metallicity range that we are concerned with in this study, nearly 20% of the stars in the MW and UFDs are CEMP stars, while the corresponding fraction of dSph sources amounts to only 6% ([Lucchesi et al. 2024](#)). The absence of CEMP stars in Cetus supports the hypothesis that the progenitor of the Cetus stream was a dSph galaxy. Otherwise, it would be highly improbable (<0.5% chance) to select a sample of 22 stars with normal carbon abundances from an UFD galaxy with a typical fraction of CEMP stars.

6.2.2. α -elements and titanium

Oxygen lines are detected in the spectra of the 12 stars with [Fe/H] > -2.2. These stars are enhanced in oxygen with respect to iron, with the average ratio [O/Fe] = 0.71 ± 0.10. This is similar to [O/Fe] = 0.7 found for the MW halo stars with [Fe/H] from -2.5 to -1.5 ([Sitnova & Mashonkina 2018](#)).

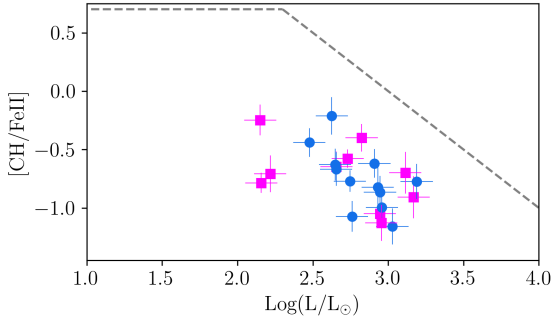


Fig. 7. $[C/Fe]$ abundance ratio as a function of luminosity. The dashed line corresponds to the empirical separation between the carbon-rich and carbon-normal populations defined by Aoki et al. (2007a). Carbon-normal stars populate the area below the dashed line. The symbols are the same as in Fig. 4.

The Cetus stars show similar enhancement in magnesium throughout the entire metallicity range, with an average ratio $[Mg/Fe] = 0.34 \pm 0.08$. This value is similar to the average values of the MP star samples in Mashonkina et al. (2019b, hereafter MN19): $[Mg/Fe] = 0.36 \pm 0.13$ from halo giants, 0.28 ± 0.07 from halo dwarfs, and 0.29 ± 0.07 from thick disk stars. A similar ratio $[Mg/Fe] = 0.30 \pm 0.11$ is observed in VMP UMi stars with $[Fe/H] < -2$, while more metal-rich UMi stars show lower $[Mg/Fe] = 0$ (Fig. 8), indicating the onset of iron production in type Ia supernovae (SNe Ia).

Our sample stars show $[Si/Fe] = 0.35 \pm 0.14$. The scatter in $[Si/Fe]$ is larger than that in $[Mg/Fe]$. This is because, for most stars, the only two lines available to determine the silicon abundance (Si I 3905 and 4102 Å) are located in the blue spectral region, which commonly suffers from low S/N and spectral line blending. If we use the eight stars that have three or more measurable Si I lines, the scatter reduces drastically to $[Si/Fe] = 0.33 \pm 0.03$. Overall, the derived ratio is close to those found by MN19 in the halo dwarfs (0.31 ± 0.07) and thick disk stars (0.26 ± 0.06).

Consistent with the magnesium and silicon, the calcium abundances in the Cetus stars exhibit an enhancement of $[Ca/Fe] = 0.37 \pm 0.08$, which is fairly similar to stars in the MN19 VMP sample: $[Ca/Fe] = 0.36 \pm 0.11$ (halo giants), 0.35 ± 0.08 (halo dwarfs), 0.24 ± 0.07 (thick disk dwarfs). The VMP UMi stars show an enhancement of $[Ca/Fe] = 0.24 \pm 0.11$ (MJ17b), and the MP stars have less enhanced $[Ca/Fe]$, following a similar trend to that found for $[Mg/Fe]$.

The source of titanium remains poorly understood, and chemical evolution models underestimate the $[Ti/Fe]$ ratio due to low nucleosynthesis yields (see e.g. Kobayashi et al. 2006, 2020). Regardless of titanium's origin, observations indicate that $[Ti/Fe]$ exhibits a similar behaviour to $[\alpha/Fe]$. The stars of our sample show $[Ti/Fe] = 0.36 \pm 0.07$, consistent with the $[Ti/Fe] = 0.33 \pm 0.07$ found in the MW halo VMP giants (MN19), as well as with the $[Mg, Si, Ca/Fe]$ ratios in the Cetus stars.

In summary, for the studied α -elements (Mg, Si, Ca), the Cetus stars consistently exhibit a similar $[\alpha/Fe] \approx 0.3$ throughout the entire metallicity range. The lack of a decreasing trend in the $[\alpha/Fe] - [Fe/H]$ diagram implies that star formation in the Cetus progenitor stopped before iron production due to SNe Ia became substantial.

6.2.3. Odd-Z elements

Figure 9 shows $[Na/Mg]$ and $[Al/Mg]$ as a function of $[Mg/H]$. The $[Na/Mg]$ ratio displays considerable scatter, while the nine

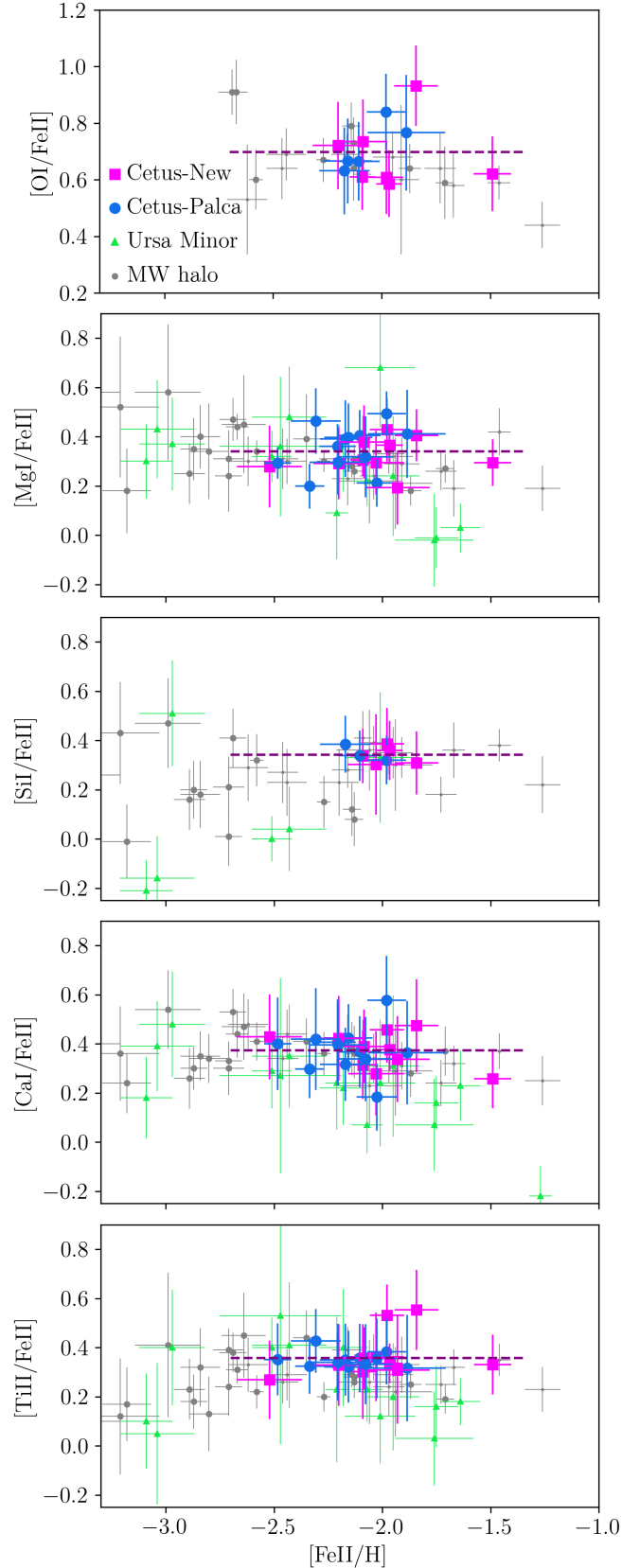


Fig. 8. NLTE abundance ratios for α -elements and titanium with respect to iron as a function of $[Fe/H]$ in the Cetus-New (magenta squares) and the Cetus-Palca (blue circles). The dashed line indicates the average element ratios in the Cetus stars. For comparison, we plotted MW halo giants (small grey circles) and dwarfs (grey dots) and UMi dSph stars (green triangles).

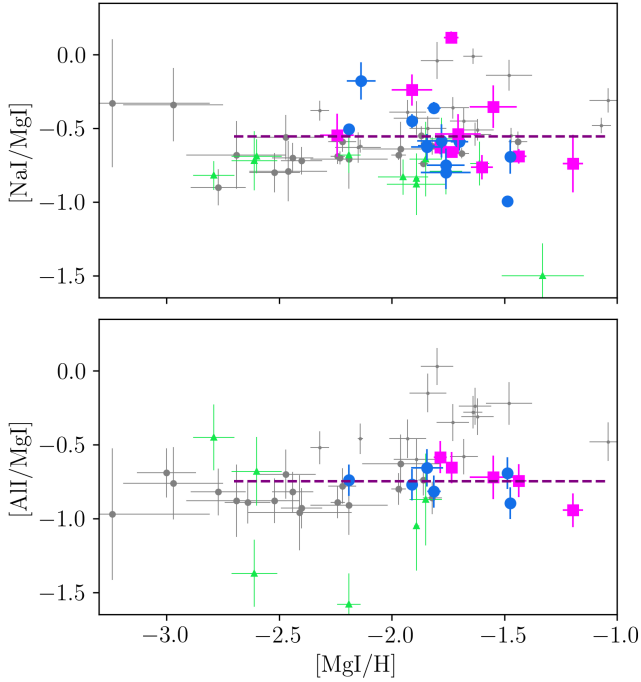


Fig. 9. NLTE abundance ratios as a function of $[Mg/H]$. The designations are the same as in Fig. 8.

stars with measured aluminium abundance show coherent ratios with an average $[Al/Mg] = -0.80 \pm 0.11$. Giants with surface gravities of $\log g < 2$ may exhibit sodium and aluminium overabundance caused by mixing and stellar evolution effects and the overabundances increase with stellar luminosity (Boyarchuk et al. 2001; Pakhomov et al. 2009; Pakhomov 2013; Alexeeva et al. 2014). Figure 10 shows $[Na/Fe]$ and $[Al/Fe]$ in our sample of stars as a function of luminosity. On average, we find $[Al/Fe] = -0.39 \pm 0.15$ and the scatter remains independent of stellar luminosity. The situation is different for sodium: the scatter in $[Na/Fe]$ increases with luminosity; although stars with normal $[Na/Fe] = -0.4$ are found across the entire luminosity range.

In our sample stars, variations in abundance due to stellar evolution impact sodium but not aluminium, and the latter can be used for galactic chemical evolution analysis. Figure 11 shows $[Al/Fe]$ as a function of $[Fe/H]$. In the MW halo, $[Al/Fe]$ rises from -0.6 to 0 with $[Fe/H]$ increasing from -3.0 to -1.5 . Unlike the stars in the MW halo, the Cetus stars do not exhibit an upward trend in $[Al/Fe]$.

Aluminium is produced by massive stars with initial masses ranging from 10 to $40 M_{\odot}$. The yields of aluminium are strongly dependent on the metallicity and the initial mass of the progenitor star, with higher CNO abundances and greater progenitor mass resulting in higher aluminium abundance (Kobayashi et al. 2006). Given the rapid stellar evolution of massive stars and the nearly instantaneous enrichment of the interstellar medium, it is more likely that the difference in $[Al/Fe]$ trends arises from a variation in the progenitor mass function rather than a variation in their metallicities. In the Cetus progenitor, the underproduction of aluminium at $[Fe/H] > -2$ could indicate a lack of the most massive stars compared to the MW. It is worth noting that only half of the stars of our sample have aluminium abundance measurements, which is due to the wavelength coverage of the observed spectra. Increasing the sample size by adding more Cetus stars with aluminium abundance determinations could

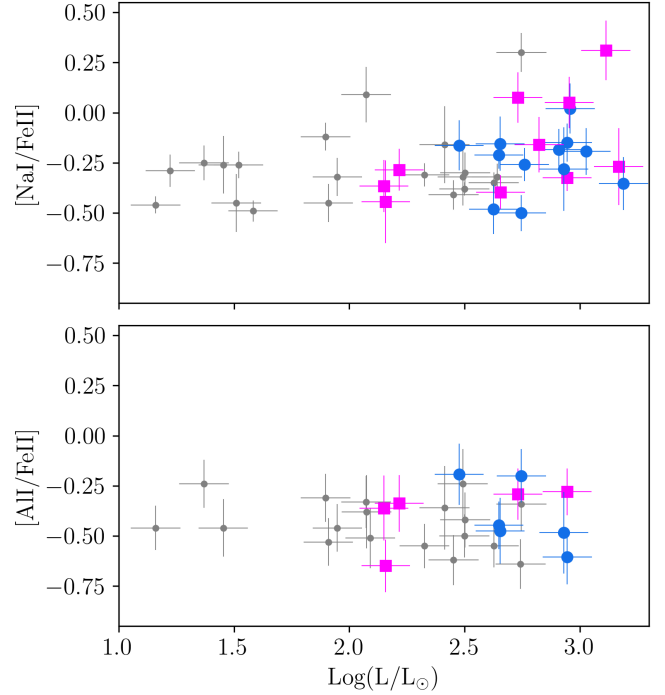


Fig. 10. NLTE abundance ratios as a function of luminosity. The designations are the same as in Fig. 8.

help us to obtain more accurate observational constraints on the $[Al/Fe]$ trend.

The origin of heavier odd-Z elements (K, Sc, V) remains poorly understood and their abundances are underestimated by chemical evolution models and stellar yields (Kobayashi et al. 2006, 2020). For these elements, our results can serve as observational constraints on chemical evolution models. We also aim to deduce how these element abundances correspond to other chemical elements. In our sample of stars, potassium, scandium, and vanadium abundances follow each other with average ratios of $[Sc/K] = 0.03 \pm 0.09$ and $[Sc/VII] = 0.08 \pm 0.16$. When calculating the $[K/Fe]$ ratio, we find $[K/Fe] = 0.11 \pm 0.12$ (Fig. 11). However, the scatter reduces significantly when comparing potassium with respect to magnesium and $[K/Mg] = -0.23 \pm 0.06$.

Following the example of Mashonkina & Romanovskaya (2022), we plot $[Sc/Ti]$ as a function of $[Fe/H]$ (Fig. 11). Our analysis of the Cetus stars reveals $[Sc/Ti] = -0.14 \pm 0.11$, which is close to the $[Sc/Ti]$ found in MW halo stars within the same $[Fe/H]$ range. The two Cetus-New stars exhibit lower $[Sc/Ti] \approx -0.4$ compared to the other stars. This is due to their higher titanium abundance with $[Ti/Fe] = 0.5$ (see Fig. 8). Maeda & Nomoto (2003) found that Sc and Ti can be produced in bipolar SNe explosions, and Sc and, to a slightly lesser extent, Ti serve as asphericity indicators of these explosions. Our results concerning the $[Sc/Ti]$ trend can be adopted as observational constraints for bipolar SNe models.

We observe an increase in $[Cu/Fe]$ from -0.8 to 0 with $[Fe/H]$ increasing from -2.5 to -1.7 . Our analysis of the MW comparison sample also reveals an increasing trend; however it is slightly shifted towards higher $[Fe/H]$ compared to the Cetus stars. Copper production is significantly influenced by metallicity – the higher the metallicity, the more copper is produced – and the MW chemical evolution models predict a rise in $[Cu/Fe]$ from -1 to 0 as $[Fe/H]$ increases from -3 to -1

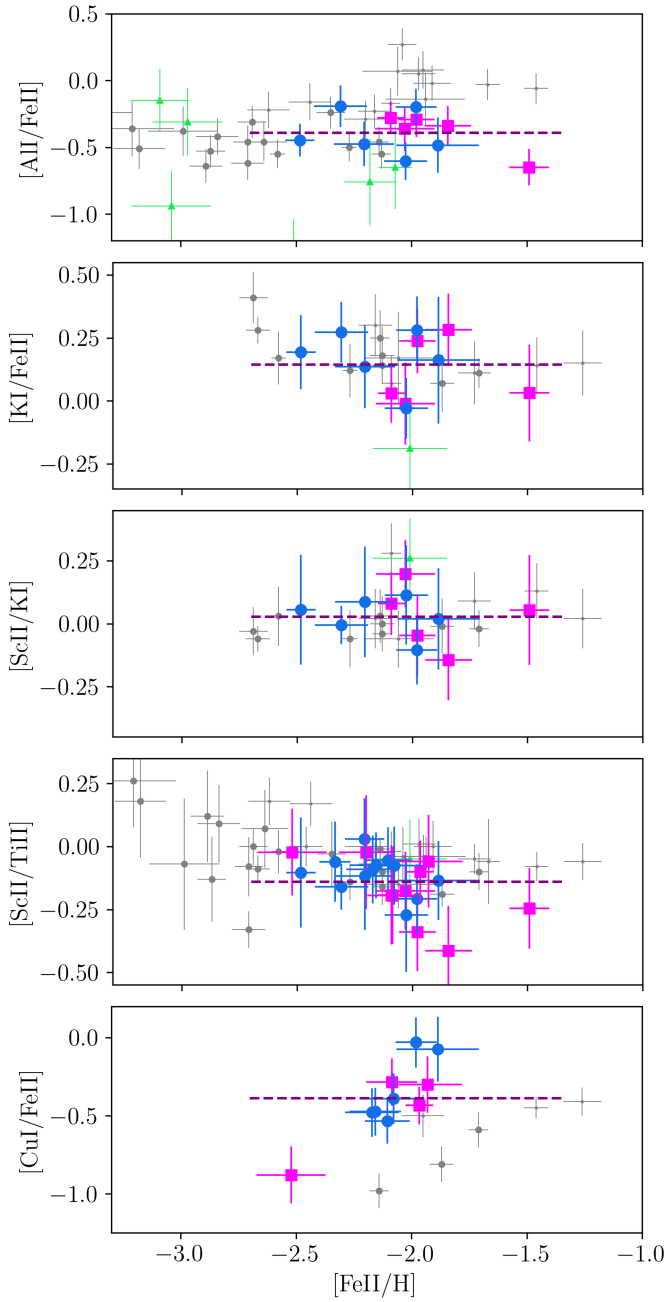


Fig. 11. NLTE abundance ratios as a function of $[\text{Fe}/\text{H}]$. The designations are the same as in Fig. 8.

(Matteucci et al. 1993; Kobayashi et al. 2006; Romano et al. 2010). Observational constraints based on NLTE studies of the MW stars generally agree on a rise in $[\text{Cu}/\text{Fe}]$ from -0.4 ± 0.1 to 0 as $[\text{Fe}/\text{H}]$ increases from -2 to -1 , while significant discrepancies in $[\text{Cu}/\text{Fe}]$ from -0.9 to -0.4 are found at $[\text{Fe}/\text{H}] < -2$ (Shi et al. 2018; Korotin et al. 2018; Andrievsky et al. 2018; Xu et al. 2022; Caffau et al. 2023). These discrepancies may arise from uncertainties in stellar atmosphere parameters or copper and iron abundances, including differences in codes, model atoms, atomic data, namely, in rate coefficients for inelastic collisions with hydrogen atoms (Xu et al. 2022; Caffau et al. 2023).

In summary, some of the most luminous stars exhibit sodium enhancements, which are potentially attributed to evolutionary changes in abundances. For odd-Z elements (Al, K, Sc), their

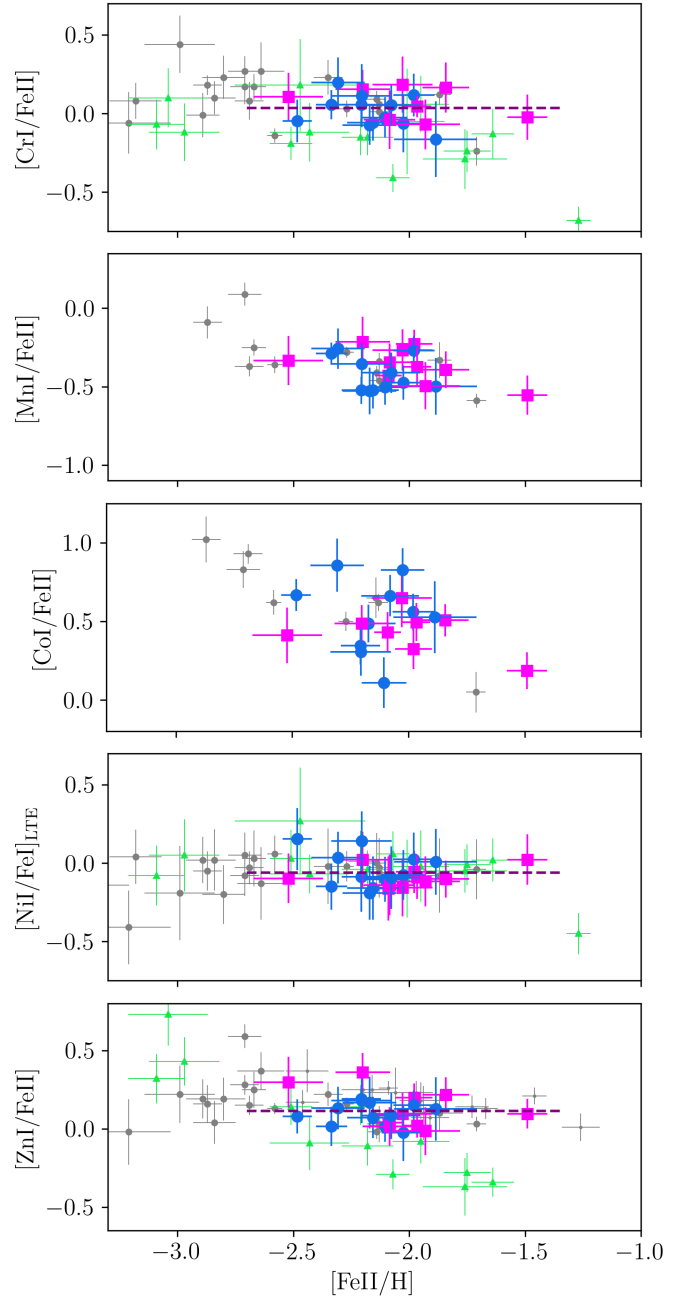


Fig. 12. NLTE abundance ratios for iron-peak elements. For Ni I, LTE abundances are plotted with respect to the LTE abundances from Fe I. The designations are the same as in Fig. 8.

$[\text{X}/\text{Fe}]$ trends are found to be flat in the Cetus stars. The limited metallicity range of the Cetus sample does not allow the detection of subtle changes in the $[\text{X}/\text{Fe}]$ ratios for these elements. An exception is $[\text{Cu}/\text{Fe}]$, where we found a prominent increase with increasing $[\text{Fe}/\text{H}]$.

6.2.4. Iron-peak elements and zinc

The $[\text{X}/\text{Fe}]$ ratios of the iron peak elements (Cr, Mn, Co, Ni) and zinc in the Cetus stars align well with those in the MW comparison sample stars with similar metallicities (Fig. 12.)

In Cetus, chromium follows iron and exhibits an average ratio of $[\text{Cr}/\text{Fe}] = 0.03 \pm 0.10$, consistent with the NLTE study of $[\text{Cr}/\text{Fe}]$ performed by Bergemann & Cescutti (2010). For

[Mn/Fe], the Cetus stars show a constant value of $[Mn/Fe] = -0.39 \pm 0.11$. Our average ratio in the Cetus and comparison sample stars is 0.2 dex lower than the nearly constant $[Mn/Fe] = -0.2$ reported for the VMP stars in the NLTE study of Bergemann et al. (2019).

Regarding [Co/Fe], the MW comparison sample shows a steep decrease of ~ 1 dex as $[Fe/H]$ increases from -2.8 to -1.7 , consistent with the earlier NLTE study of Bergemann et al. (2010). The [Co/Fe] trend in Cetus is consistent with that in the MW (Fig. 12). However, the scatter in Cetus is larger and can be attributed to the uncertainties in the observed spectra: the two lines of Co I at 4110 and 4121 Å are available for abundance determination and they are displaced in the blue spectral region, where the S/N is lower compared to the red region.

For nickel, our determinations rely on the LTE analysis. We assume that the NLTE effects are nearly the same for Ni I and Fe I and analyse the $[Ni I/Fe I]_{LTE}$ ratio, where both Ni I and Fe I abundances are taken in LTE. Using the same approach, M17b found a solar value of $[Ni/Fe]$ for the VMP stars in the MW halo and dwarf galaxies. We find the same result for the Cetus stars with an average $[Ni I/Fe I]_{LTE} = -0.06 \pm 0.09$. For Cetus stars, on average, we find $[Zn/Fe] = 0.11 \pm 0.10$, in agreement with the MW comparison sample stars with similar metallicities. In summary, nucleosynthesis in massive stars appears to be the primary source of iron-peak elements and zinc in the Cetus stars, with no clear evidence of a contribution from SNe Ia.

6.2.5. Neutron capture elements

We adopt a commonly accepted opinion on the origin of neutron capture (n-capture) elements in rapid (r-) and slow (s-) neutron capture processes. Europium is a typical r-element and is almost totally synthesised via the r-process. Its site and nuclear reactions branching along its path are debated (e.g. see Cowan et al. 2021). Barium is known as an s-element, as 81% of the barium in the matter of the Solar System originates from the main s-process, which takes place in the low- to intermediate-mass ($1-6 M_{\odot}$) AGB stars (Arlandini et al. 1999; Busso et al. 1999; Bisterzo et al. 2011; Lugaro et al. 2012). The r-process also produces a certain amount of barium.

For light n-capture elements (Sr, Y, Zr), observations of VMP stars with supersolar $[Sr/Ba]$ ratios and $[Ba/H] < -2.5$ suggest the existence of an additional production channel besides the r-process and the main s-process (Travaglio et al. 2004). Its nuclear reactions and astrophysical sites are not yet known, while many hypotheses have been suggested (for their discussion and references, see Sect. 5.4 in M17b). It is important to highlight that the suggested sources share a common signature: they efficiently produce the light s-process elements (Sr, Y, Zr), while the production of barium either does not occur, as in the weak s-process (Raiteri et al. 1991), or occurs to a much lesser degree, as in fast rotating massive stars (Frischnecht et al. 2016; Limongi & Chieffi 2018) or in the intermediate (i-)process occurring in rapidly accreting white dwarfs (Côté et al. 2018) and AGB stars with masses ranging from 1 to $4 M_{\odot}$ (Choplin et al. 2024).

The upper panel of Fig. 13 shows $[Ba/Mg]$ as a function of $[Mg/H]$. Magnesium, originating primarily from massive stars, can serve as a benchmark element for VMP stars, in contrast to iron, which stems from stars of various masses. In the Appendix, we present conventional diagrams employing iron as the reference element. The Cetus stars have $[Mg/H] > -2.2$ and exhibit a flat $[Ba/Mg]$ trend with an average ratio $[Ba/Mg] = -0.51 \pm 0.20$. This value aligns well with the $[Ba/Mg]$ ratio in the MW halo stars with similar $[Mg/H]$. For $[Mg/H] < -2.3$, the MW halo

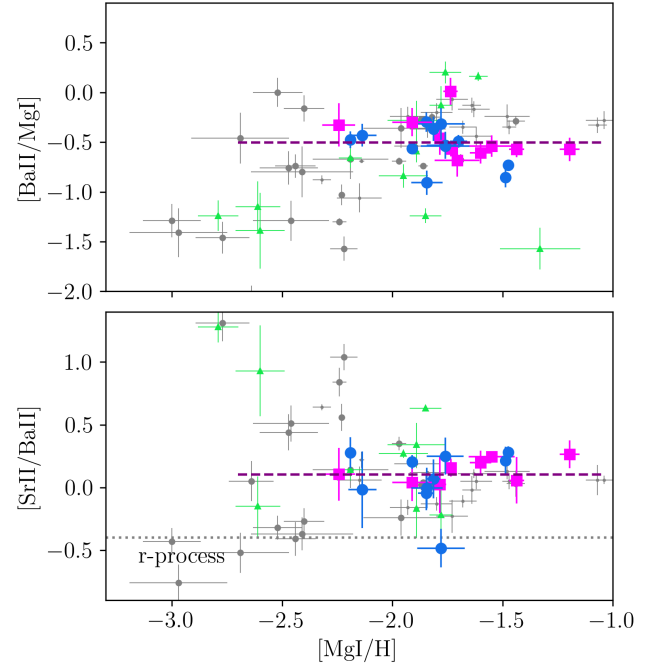


Fig. 13. Neutron capture element abundance ratios. The dotted line indicates the empirical r-process ratios observed in r-II type stars. The designations are the same as in Fig. 8.

stars exhibit an increase in $[Ba/Mg]$ as $[Mg/H]$ rises, although there is substantial scatter of $[Ba/Mg]$, namely from -1.5 to 0 . Our Cetus sample lacks stars with $[Mg/H] < -2.3$ and does not allow us to track its earliest stages.

To understand the sources responsible for n-capture element production within different regimes, let us take a look at the $[Sr/Ba] - [Mg/H]$ diagram (Fig. 13, bottom panel). The Cetus stars exhibit a nearly solar $[Sr/Ba]$ ratio with an average $[Sr/Ba] = 0.10 \pm 0.18$, in line with the MW halo stars with similar $[Mg/H]$. The MW halo stars with $[Mg/H] < -2.2$ show a dispersion of 2 dex in $[Sr/Ba]$, with a minimum value at $[Sr/Ba]_r = -0.4$. The latter value is known as an empirical r-process ratio observed in stars strongly enhanced in r-process elements (Snedden et al. 2003; Barklem et al. 2005; Hayek et al. 2009; Mashonkina et al. 2010; Roederer et al. 2018; Shah et al. 2024). The supersolar $[Sr/Ba]$ ratios in stars with $[Mg/H] < -2.2$ are due to the contribution to Sr from an additional source(s) of unknown nature, as discussed earlier.

The Cetus stars do not exhibit substantially supersolar $[Sr/Ba]$ ratios. One possibility explaining this situation could be that the stars were formed after completing that additional source in the Cetus progenitor; another possibility is that the source of unknown nature did not run at all. Further observations and increased statistics of Cetus VMP stars with $[Mg/H] < -2.3$ are needed to study its earliest epochs.

For our sample stars, we estimate the contribution of the r-process to their chemical composition using their $[Eu/Ba]$ ratios. Figure 14 shows $[Eu/Ba]$ as a function of $[Ba/H]$. We find an average value $[Eu/Ba] = 0.53 \pm 0.13$. This ratio is between the solar value and the r-process $[Eu/Ba]_r = 0.80$ (Bisterzo et al. 2014, here the r-residual is defined as the difference between solar total and s-process abundance). Our average value $[Eu/Ba]_{Cetus} \approx 0.5$ indicates that the Eu to Ba number density ratio in r-process material is twice ($10^{0.3}$) that in the Cetus stars. In other words, on average, half of the barium is produced

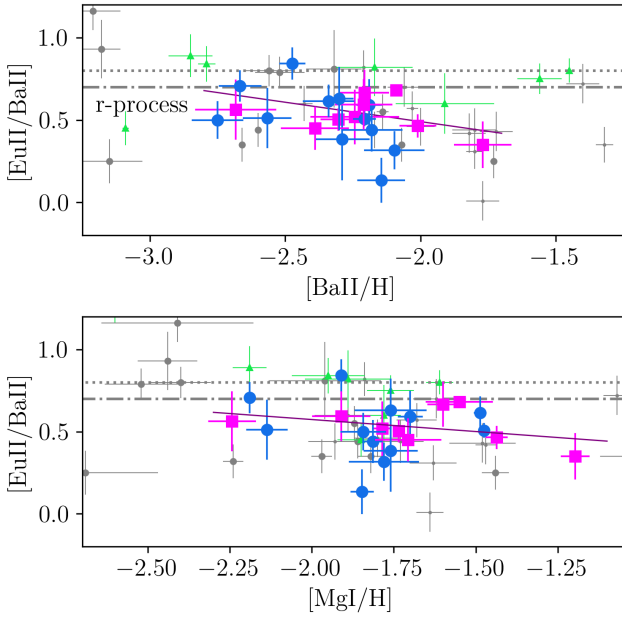


Fig. 14. Neutron capture element abundance ratios. The predicted r-process element ratios are shown with the dotted line (Arlandini et al. 1999) and dashdotted line (Bisterzo et al. 2014). The solid line represents a linear regression of the trend. The designations are the same as in Fig. 8.

in the r-process. This estimate is close to the s-process contribution of $30\% \pm 30\%$ to barium in metal-poor thick-disk stars, as found by Mashonkina et al. (2003).

In different Cetus stars, [Eu/Ba] takes values from -0.1 to 0.8 , corresponding to r-process contributions ranging from 20% to 100% , respectively. We note a decreasing trend in [Eu/Ba] relative to [Ba/H] (Fig. 14). We find this trend to be statistically significant with a slope of -0.23 ± 0.14 and a p -value of 0.06 . In other words, assuming a decrease in the [Eu/Ba] – [Ba/H] diagram, there is only a 6% chance that our hypothesis is wrong.

Figure 14 (bottom panel) also shows [Eu/Ba] as a function of [Mg/H]. In the latter case, the decreasing trend is less pronounced, with a slope of -0.16 ± 0.11 and a p -value of 0.11 . Nevertheless, we can conclude that, as metallicity or [Mg/H] increases, the barium production rate grows relative to that for europium, suggesting an increasing contribution from the s-process in AGB stars. We also note a scatter of [Eu/Ba], indicating that the interstellar medium in the Cetus progenitor was not fully mixed.

In Cetus, we find the trend in [Eu/Ba] to be consistent with that in the MW halo indicating a similar relative contribution from AGB stars in these two systems at the [Ba/H] ranging from -2.7 to -1.8 . In our sample of UMi comparison stars, the r-process dominates and stars with [Ba/H] of -1.5 still exhibit close to r-process [Eu/Ba] ratios of 0.7 . A different situation was found by Skúladóttir et al. (2020) from an n-capture element abundance analysis in Sculptor (Scl) dSph, a dwarf galaxy with a stellar mass of $10^6 m_{\odot}$, which is close to that of the Cetus and UMi. Stars in Scl with [Ba/H] > -1.5 exhibit lower [Y,La,Nd,Eu/Ba] compared to the MW halo stars, suggesting a higher relative contribution from AGB stars at these [Ba/H]. The distinct trends observed in these systems can be explained by their different star formation histories. In the Cetus progenitor, within the studied metallicity range, the star formation history was similar to that in the MW halo. It is worth noting that, in

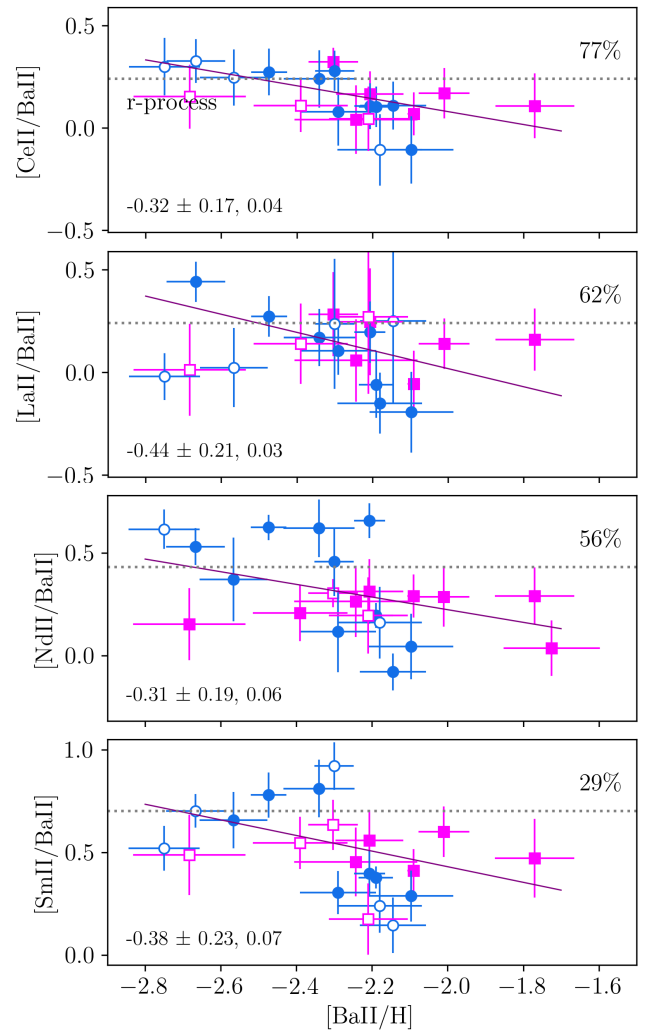


Fig. 15. Neutron capture element abundance ratios. The solid line represents a linear regression of the trend. For each trend, the slope and the corresponding p -value are indicated. The dotted line indicates the empirical r-process ratios observed in r-II type stars; see text for details. Open symbols represent stars with less reliable abundance measurements. The fraction of s-nuclei in the Solar System is indicated for each element. The designations are the same as in Fig. 8.

Scl, [Ba/H] spans a wide range up to [Ba/H] = -0.5 , while in our Cetus sample, [Ba/H] reaches -1.8 .

Besides barium, the main s-process produces effectively second peak s-process elements such as cerium, lanthanum, neodymium, and samarium. The Solar System s-nuclei fractions for these elements are 77 , 62 , 65 , and 29% , respectively (Arlandini et al. 1999). However, their production in the main s-process is less effective compared to barium, which has an s-nuclei fraction of 81% in the Solar System.

Relative contributions of the s- and r-processes to chemical abundances of the Cetus stars can be drawn by plotting the abundance ratios for the n-capture elements with different contributions of the s- and r-processes to their solar abundances with respect to barium. As seen in Fig. 15, each of the four elements (Ce, La, Nd, Sm) shows statistically significant decreasing trends as barium increases, indicating an increasing contribution from the s-process in AGB stars. The slopes and p -values are quoted in the corresponding panels of Fig. 15. For [Ba/H] > -2.2 , the [Ce, La, Nd, Sm/Ba] ratios decrease below the empirical

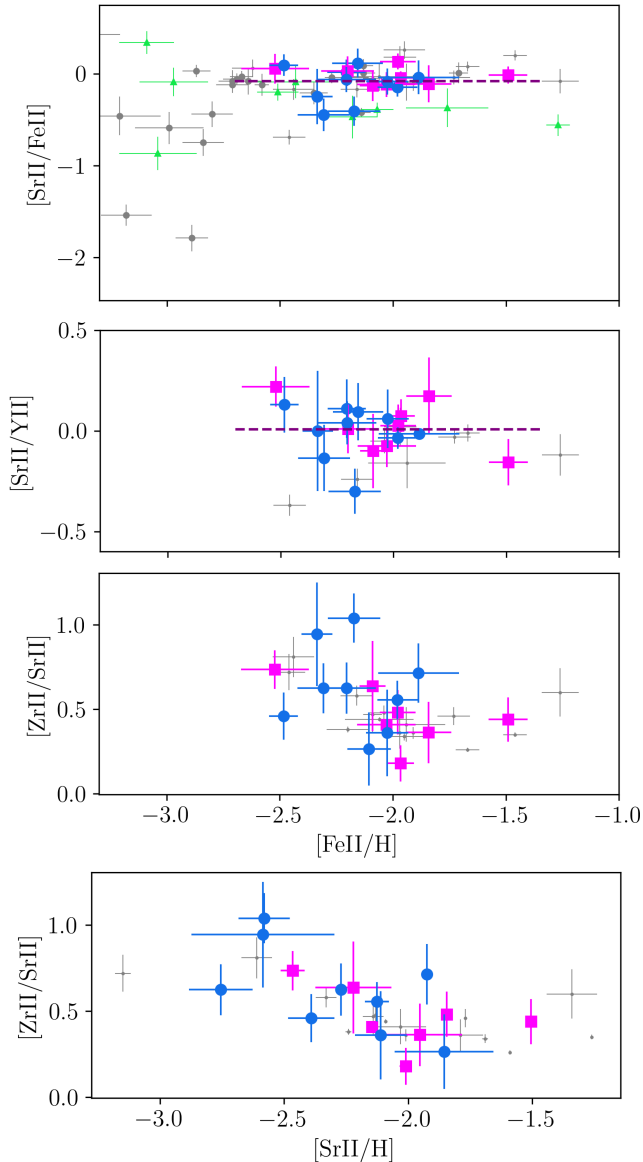


Fig. 16. Abundance ratios for light neutron-capture elements. The designations are the same as in Fig. 8.

r-process ratios calculated for the r-II stars using the data from Sneden et al. (2003), Barklem et al. (2005), Hayek et al. (2009), Mashonkina et al. (2010), Roederer et al. (2018), and Shah et al. (2024).

Examining the diagrams more closely, we note a hint of distinct behaviour between the Cetus-New and Cetus-Palca stars. The Cetus-Palca stars show a prominent decrease with a variation of about 0.5 dex in abundance ratios, while the Cetus-New trends remain almost flat. However, this impression mainly relies on three Cetus-New stars – two with $[\text{Ba}/\text{H}] \geq -2.0$ and one with $[\text{Ba}/\text{H}] = -2.7$. Therefore, our current statistics do not allow us to draw solid conclusions about the distinct behaviour of n-capture elements in the two wraps.

In both the Cetus stream and the MW comparison sample, the $[\text{Sr}/\text{Y}]$ trend is flat (Fig. 16), with values close to the solar ratio, indicating similar production rates for these light n-capture elements. The situation is different for $[\text{Zr}/\text{Sr}]$, which ranges from about 0.2 dex to 1 dex in the Cetus stars. These ratios may look like a scatter in the diagrams versus metallicity

$[\text{Fe}/\text{H}]$, while they form a clear declining trend in the plot against $[\text{Sr}/\text{H}]$ (Fig. 16). The latter suggests that the Cetus stars formed in the environment with a higher production rate for strontium and yttrium compared to that for zirconium. This is one more argument for the onset of the main s-process in the Cetus progenitor, because zirconium is less efficiently produced in the main s-process compared to strontium and yttrium. The corresponding contributions of Sr, Y, and Zr to the Solar System amount to 71%, 69%, and 65%, respectively (main s-process, Travaglio et al. 2004). In the MW halo, an increase in $[\text{Zr}/\text{Sr}]$ and $[\text{Zr}/\text{Y}]$ towards lower metallicity was reported by Zhao et al. (2016) and Alexeeva et al. (2023), respectively, while the $[\text{Zr}/\text{Sr}]$ plateau was found by Lombardo et al. (2022) for their MW stellar sample.

From analyses of the $[\text{Sr}/\text{Ba}]$ and $[\text{Sr}/\text{Y}]$, we conclude that strontium, yttrium, and barium in the Cetus stars have a common nucleosynthetic origin from the r-process and the main s-process. Zirconium in the Cetus stars behaves distinctly, indicating its less effective production in the main s-process compared to the above elements.

In summary, the n-capture elements in the Cetus stars originate from both the r-process and the main s-process. In the different stars of our sample, the contribution from these two processes is different, and, for example, for barium, the r/s ratio varies from 100%/0% to 20%/80% with an average value of 50%/50%.

7. Conclusions

We provide a comprehensive analysis of the chemical composition of 22 stars in the Cetus stream based on their high-resolution spectra. The abundances are derived by taking into account NLTE effects if possible. In total, we determined abundances for up to 28 chemical species from C to Dy and account for the NLTE effects for 20 of them. We summarise the conclusions we draw from the derived abundances below.

- The Cetus stars cover a metallicity $[\text{Fe}/\text{H}]$ range from -2.5 to -1.5 . The mean metallicity of the stream is $[\text{Fe}/\text{H}] = -2.11 \pm 0.21$. The chemical compositions of the Cetus-New and Cetus-Palca wraps suggests that both follow the same chemical evolution path.
- All sample stars are α enhanced with $[\alpha/\text{Fe}] = 0.3$. The absence of a ‘knee’ in the $[\alpha/\text{Fe}] - [\text{Fe}/\text{H}]$ diagram indicates that star formation stopped before iron production due to SNe Ia became substantial.
- Neutron capture element abundances suggest that both r-process and main s-process contributed to their origin. The decrease in $[\text{Eu}/\text{Ba}]$ from a typical r-process value $[\text{Eu}/\text{Ba}] = 0.7$ to 0.3 with increasing $[\text{Ba}/\text{H}]$ indicates a distinct contribution of the r- and s-processes to the chemical composition of different Cetus stars. For barium, the r-process contribution varies from 100 to 20% in different sample stars, with an average value of 50%.
- Star formation in the Cetus progenitor ceased after the onset of the main s-process in low-intermediate-mass AGB stars, but before SNe Ia played an important role in the chemical enrichment of the galaxy.

When comparing the abundance ratios of the Cetus stream with the MW halo, we observe that, in the same metallicity range, these two samples generally align. It is essential to bear in mind that MW halo stars exhibit a much broader range of abundance ratios, given the vast and complex origins of the MW halo. Regarding the observed differences, the most notable discrepancy is found in the $[\text{Cu}/\text{Fe}] - [\text{Fe}/\text{H}]$ trends: in Cetus, it is shifted by 0.5 dex towards lower $[\text{Fe}/\text{H}]$ compared to the MW trend.

Regarding our comparison with the UMi dSph, we observe significant differences between these two systems. In contrast to Cetus, UMi stars exhibit a ‘knee’ in $[\alpha/\text{Fe}]$, which we can use as an indicator of the onset of contributions from SNe Ia. This implies that UMi dSph has a more extended star formation history compared to Cetus. This finding aligns with the estimates of Naidu et al. (2022), who found the star formation quenching redshift in Cetus to be larger than that in the UMi dSph. Regarding neutron capture elements, UMi stars display a diversity, including strongly r-process-enhanced stars, stars with overabundances in light n-capture elements, and stars with contributions from the main s-process. The distinct features in elemental abundances between these two systems with similar stellar mass show that the star formation histories in low-mass dwarf galaxies are not as simple as what we would probably expect. Instead, the diversity and uniqueness of each system can be revealed by their detailed chemical compositions.

This work shows that the high-resolution spectra for a stellar stream allow us to reveal the origins of the elements in a low-mass dwarf galaxy and, moreover, quantify their relative contributions from different production channels. Combining the knowledge from nucleosynthesis predictions, we are able to constrain the star formation history of the progenitor dwarf galaxy. This is the first work in the HR-GO series, and the detailed abundances of more stellar streams and substructures will be systematically analysed in the coming papers. Ultimately, we will obtain a sample of dwarf galaxies with diverse evolution histories based on the library of stellar debris in the MW.

8. Data availability

The full Tables 2 and 4 are available at the CDS via anonymous ftp to cdsarc.cds.unistra.fr (130.79.128.5) or via <https://cdsarc.cds.unistra.fr/viz-bin/cat/J/A+A/690/A331>.

The list of sample stars and their kinematical properties is provided by Z. Yuan at <https://zenodo.org/records/13334600>.

Acknowledgements. The authors are indebted to T. Li, A. Bonaca, K. Venn for their assistance in getting the observed spectra. T.S. is grateful to Yu. V. Pakhomov for providing his code for echelle orders merging. The authors thank the referee for carefully reading the manuscript and providing valuable feedback. L.L. acknowledges the support by the State of Hesse within the Research Cluster ELEMENTS (Project ID 500/10.006). N.F.M. gratefully acknowledge support from the French National Research Agency (ANR) funded project ‘‘Pristine’’ (ANR-18-CE31-0017) along with funding from the European Research Council (ERC) under the European Unions Horizon 2020 research and innovation programme (grant agreement No. 834148). This research is based in part on data collected at the Subaru Telescope, which is operated by the National Astronomical Observatory of Japan. We are honoured and grateful for the opportunity of observing the Universe from Maunakea, which has the cultural, historical, and natural significance in Hawaii. This work has made use of data from the European Space Agency mission *Gaia* (<https://www.cosmos.esa.int/gaia>), processed by the *Gaia* Data Processing and Analysis Consortium (DPAC, <https://www.cosmos.esa.int/web/gaia/dpac/consortium>). We present the Source IDs, distances, as well as the abundances and the equivalent widths for individual lines of the Cetus member stars in the HR-GO program.

References

Aguado, D. S., Belokurov, V., Myeong, G. C., et al. 2021, *ApJ*, 908, L8
 Alexeeva, S. A., & Mashonkina, L. I. 2015, *MNRAS*, 453, 1619
 Alexeeva, S. A., Pakhomov, Y. V., & Mashonkina, L. I. 2014, *Astron. Lett.*, 40, 406
 Alexeeva, S., Wang, Y., Zhao, G., et al. 2023, *ApJ*, 957, 10
 Andrievsky, S., Bonifacio, P., Caffau, E., et al. 2018, *MNRAS*, 473, 3377
 Aoki, W., Beers, T. C., Christlieb, N., et al. 2007a, *ApJ*, 655, 492

Aoki, W., Honda, S., Sadakane, K., & Arimoto, N. 2007b, *PASJ*, 59, L15
 Arlandini, C., Käppeler, F., Wisshak, K., et al. 1999, *ApJ*, 525, 886
 Bailer-Jones, C. A. L. 2015, *PASP*, 127, 994
 Bailer-Jones, C. A. L., Rybizki, J., Fousneau, M., Demleitner, M., & Andrae, R. 2021, *AJ*, 161, 147
 Balbinot, E., Cabrera-Ziri, I., & Lardo, C. 2022, *MNRAS*, 515, 5802
 Barklem, P. S., Christlieb, N., Beers, T. C., et al. 2005, *A&A*, 439, 129
 Bergemann, M., & Cescutti, G. 2010, *A&A*, 522, A9
 Bergemann, M., Pickering, J. C., & Gehren, T. 2010, *MNRAS*, 401, 1334
 Bergemann, M., Gallagher, A. J., Eitner, P., et al. 2019, *A&A*, 631, A80
 Bergemann, M., Hoppe, R., Semanova, E., et al. 2021, *MNRAS*, 508, 2236
 Bernstein, R., Shectman, S. A., Gunnels, S. M., Mochmacki, S., & Athey, A. E. 2003, *SPIE Conf. Ser.*, 4841, 1694
 Bisterzo, S., Gallino, R., Straniero, O., Cristallo, S., & Käppeler, F. 2011, *MNRAS*, 418, 284
 Bisterzo, S., Travaglio, C., Gallino, R., Wiescher, M., & Käppeler, F. 2014, *ApJ*, 787, 10
 Boyarchuk, A. A., Antipova, L. I., Boyarchuk, M. E., & Savanov, I. S. 2001, *Astron. Rep.*, 45, 301
 Bruls, J. H. M. J. 1993, *A&A*, 269, 509
 Busso, M., Gallino, R., & Wasserburg, G. J. 1999, *ARA&A*, 37, 239
 Butler, K. 1984, Ph.D. Thesis, University of London, UK
 Caffau, E., Lombardo, L., Mashonkina, L., et al. 2023, *MNRAS*, 518, 3796
 Casagrande, L., & Vandenberg, D. A. 2018, *MNRAS*, 479, L102
 Ceccarelli, E., Massari, D., Mucciarelli, A., et al. 2024, *A&A*, 684, A37
 Chandra, V., Conroy, C., Caldwell, N., et al. 2022, *ApJ*, 940, 127
 Chang, J., Yuan, Z., Xue, X.-X., et al. 2020, *ApJ*, 905, 100
 Choplin, A., Siess, L., Goriely, S., & Martinet, S. 2024, *A&A*, 684, A206
 Cohen, J. G., & Huang, W. 2010, *ApJ*, 719, 931
 Côté, B., Denissenkov, P., Herwig, F., et al. 2018, *ApJ*, 854, 105
 Cowan, J. J., Sneden, C., Lawler, J. E., et al. 2021, *Rev. Mod. Phys.*, 93, 015002
 Cui, X.-Q., Zhao, Y.-H., Chu, Y.-Q., et al. 2012, *Res. Astron. Astrophys.*, 12, 1197
 Dekker, H., D’Odorico, S., Kaufer, A., Delabre, B., & Kotzlowski, H. 2000, *SPIE Conf. Ser.*, 4008, 534
 Deng, L.-C., Newberg, H. J., Liu, C., et al. 2012, *Res. Astron. Astrophys.*, 12, 735
 Dotter, A. 2016, *ApJS*, 222, 8
 Dotter, A., Chaboyer, B., Jevremović, D., et al. 2008, *ApJS*, 178, 89
 Eitner, P., Bergemann, M., Ruitter, A. J., et al. 2023, *A&A*, 677, A151
 Frischknecht, U., Hirschi, R., Pignatari, M., et al. 2016, *MNRAS*, 456, 1803
 Gaia Collaboration (Brown, A. G. A., et al.) 2021, *A&A*, 649, A1
 Giddings, J. 1981, Ph.D. Thesis, University of London, UK
 Grevesse, N., & Sauval, A. J. 1999, *A&A*, 347, 348
 Gull, M., Frebel, A., Hinojosa, K., et al. 2021, *ApJ*, 912, 52
 Gustafsson, B., Edvardsson, B., Eriksson, K., et al. 2008, *A&A*, 486, 951
 Hawkins, K., Price-Whelan, A. M., Sheffield, A. A., et al. 2023, *ApJ*, 948, 123
 Hayek, W., Wiesendahl, U., Christlieb, N., et al. 2009, *A&A*, 504, 511
 Huang, Y., Beers, T. C., Wolf, C., et al. 2022, *ApJ*, 925, 164
 Ibata, R., Malhan, K., Martin, N., et al. 2021, *ApJ*, 914, 123
 Ibata, R., Malhan, K., Tenachi, W., et al. 2024, *ApJ*, 967, 89
 Jablonka, P., North, P., Mashonkina, L., et al. 2015, *A&A*, 583, A67
 Ji, A. P., Li, T. S., Hansen, T. T., et al. 2020a, *AJ*, 160, 181
 Ji, A. P., Li, T. S., Simon, J. D., et al. 2020b, *ApJ*, 889, 27
 Ji, A. P., Naidu, R. P., Brauer, K., Ting, Y.-S., & Simon, J. D. 2023, *MNRAS*, 519, 4467
 Kelson, D. D. 2003, *PASP*, 115, 688
 Kirby, E. N., & Cohen, J. G. 2012, *AJ*, 144, 168
 Kirby, E. N., Cohen, J. G., Guhathakurta, P., et al. 2013, *ApJ*, 779, 102
 Kobayashi, C., Umeda, H., Nomoto, K., Tominaga, N., & Ohkubo, T. 2006, *ApJ*, 653, 1145
 Kobayashi, C., Karakas, A. I., & Lugaro, M. 2020, *ApJ*, 900, 179
 Kochukhov, O. 2018, Astrophysics Source Code Library [[record ascl:1805.015](https://ui.adsabs.org/abs/2018ASCl..1805..015K)]
 Korotin, S. A., Andrievsky, S. M., & Zhukova, A. V. 2018, *MNRAS*, 480, 965
 Li, T. S., Ji, A. P., Pace, A. B., et al. 2022, *ApJ*, 928, 30
 Limberg, G., Santucci, R. M., Rossi, S., et al. 2021, *ApJ*, 913, L28
 Limberg, G., Ji, A. P., Naidu, R. P., et al. 2024, *MNRAS*, 530, 2512
 Limongi, M., & Chieffi, A. 2018, *ApJS*, 237, 13
 Lind, K., Nordlander, T., Wehrhahn, A., et al. 2022, *A&A*, 665, A33
 Lindegren, L., Bastian, U., Biermann, M., et al. 2021, *A&A*, 649, A4
 Liu, C., Deng, L.-C., Carlin, J. L., et al. 2014, *ApJ*, 790, 110
 Loders, K. 2021, *Space Sci. Rev.*, 217, 44
 Lombardo, L., Bonifacio, P., François, P., et al. 2022, *A&A*, 665, A10
 Lucchesi, R., Jablonka, P., Skúladóttir, Á., et al. 2024, *A&A*, 686, A266
 Lugaro, M., Karakas, A. I., Stancliffe, R. J., & Rijs, C. 2012, *ApJ*, 747, 2
 Maeda, K., & Nomoto, K. 2003, *ApJ*, 598, 1163
 Magg, E., Bergemann, M., Serenelli, A., et al. 2022, *A&A*, 661, A140
 Martin, N. F., Ibata, R. A., Starkenburg, E., et al. 2022a, *MNRAS*, 516, 5331

- Martin, N. F., Venn, K. A., Aguado, D. S., et al. 2022b, *Nature*, **601**, 45
- Mashonkina, L. 2013, *A&A*, **550**, A28
- Mashonkina, L. I., & Belyaev, A. K. 2019, *Astron. Lett.*, **45**, 341
- Mashonkina, L., & Gehren, T. 2000, *A&A*, **364**, 249
- Mashonkina, L. I., & Romanovskaya, A. M. 2022, *Astron. Lett.*, **48**, 455
- Mashonkina, L., Gehren, T., Travaglio, C., & Borkova, T. 2003, *A&A*, **397**, 275
- Mashonkina, L., Christlieb, N., Barklem, P. S., et al. 2010, *A&A*, **516**, A46
- Mashonkina, L., Gehren, T., Shi, J.-R., Korn, A. J., & Grupp, F. 2011, *A&A*, **528**, A87
- Mashonkina, L. I., Belyaev, A. K., & Shi, J. R. 2016, *Astron. Lett.*, **42**, 366
- Mashonkina, L., Jablonka, P., Pakhomov, Y., Sitnova, T., & North, P. 2017a, *A&A*, **604**, A129
- Mashonkina, L., Jablonka, P., Sitnova, T., Pakhomov, Y., & North, P. 2017b, *A&A*, **608**, A89
- Mashonkina, L., Sitnova, T., & Belyaev, A. K. 2017c, *A&A*, **605**, A53
- Mashonkina, L., Sitnova, T., Yakovleva, S. A., & Belyaev, A. K. 2019a, *A&A*, **631**, A43
- Mashonkina, L. I., Neretina, M. D., Sitnova, T. M., & Pakhomov, Y. V. 2019b, *Astron. Rep.*, **63**, 726
- Mashonkina, L., Pakhomov, Y. V., Sitnova, T., et al. 2022, *MNRAS*, **509**, 3626
- Mashonkina, L., Pakhomov, Y., Sitnova, T., et al. 2023, *MNRAS*, **524**, 3526
- Matsuno, T., Dodd, E., Koppelman, H. H., et al. 2022a, *A&A*, **665**, A46
- Matsuno, T., Koppelman, H. H., Helmi, A., et al. 2022b, *A&A*, **661**, A103
- Matteucci, F., Raiteri, C. M., Busson, M., Gallino, R., & Gratton, R. 1993, *A&A*, **272**, 421
- McConnachie, A. W. 2012, *AJ*, **144**, 4
- Mighell, K. J., & Burke, C. J. 1999, *AJ*, **118**, 366
- Mucciarelli, A., Bellazzini, M., & Massari, D. 2021, *A&A*, **653**, A90
- Naidu, R. P., Conroy, C., Bonaca, A., et al. 2022, arXiv e-prints [arXiv:2204.09057]
- Neretina, M. D., Mashonkina, L. I., Sitnova, T. M., Yakovleva, S. A., & Belyaev, A. K. 2020, *Astron. Lett.*, **46**, 621
- Newberg, H. J., Yanny, B., & Willett, B. A. 2009, *ApJ*, **700**, L61
- Noguchi, K., Aoki, W., Kawanomoto, S., et al. 2002, *PASJ*, **54**, 855
- Pakhomov, Y. V. 2013, *Astron. Lett.*, **39**, 54
- Pakhomov, Y. V., Antipova, L. I., Boyarchuk, A. A., et al. 2009, *Astron. Rep.*, **53**, 660
- Pakhomov, Y. V., Ryabchikova, T. A., & Piskunov, N. E. 2019, *Astron. Rep.*, **63**, 1010
- Placco, V. M., Frebel, A., Beers, T. C., & Stancliffe, R. J. 2014, *ApJ*, **797**, 21
- Popa, S. A., Hoppe, R., Bergemann, M., et al. 2023, *A&A*, **670**, A25
- Raassen, A. J. J., & Uylings, P. H. M. 1998, *A&A*, **340**, 300
- Raiteri, C. M., Busso, M., Gallino, R., Picchio, G., & Pulone, L. 1991, *ApJ*, **367**, 228
- Reggiani, H., Schlafman, K. C., & Casey, A. R. 2023, *AJ*, **166**, 128
- Roederer, I. U., & Gnedin, O. Y. 2019, *ApJ*, **883**, 84
- Roederer, I. U., Sneden, C., Thompson, I. B., Preston, G. W., & Shectman, S. A. 2010, *ApJ*, **711**, 573
- Roederer, I. U., Sakari, C. M., Placco, V. M., et al. 2018, *ApJ*, **865**, 129
- Romano, D., Karakas, A. I., Tosi, M., & Matteucci, F. 2010, *A&A*, **522**, A32
- Ryabchikova, T., Piskunov, N., Kurucz, R. L., et al. 2015, *Phys. Scr.*, **90**, 054005
- Sadakane, K., Arimoto, N., Ikuta, C., et al. 2004, *PASJ*, **56**, 1041
- Schlafly, E. F., & Finkbeiner, D. P. 2011, *ApJ*, **737**, 103
- Sestito, F., Zarella, D., Venn, K. A., et al. 2023, *MNRAS*, **525**, 2875
- Shah, S. P., Ezzeddine, R., Roederer, I. U., et al. 2024, *MNRAS*, **529**, 1917
- Shetrone, M. D., Côté, P., & Sargent, W. L. W. 2001, *ApJ*, **548**, 592
- Shi, J. R., Yan, H. L., Zhou, Z. M., & Zhao, G. 2018, *ApJ*, **862**, 71
- Shipp, N., Drlica-Wagner, A., Balbinot, E., & Ferguson, P. 2018, *ApJ*, **862**, 114
- Sitnova, T. M., & Mashonkina, L. I. 2018, *Astron. Lett.*, **44**, 411
- Sitnova, T., Zhao, G., Mashonkina, L., et al. 2015, *ApJ*, **808**, 148
- Sitnova, T. M., Mashonkina, L. I., Przybilla, N., & Kamp, I. 2018, in *A.A. Boyarchuk Memorial Conference*, eds. D. V. Bisikalo, & D. S. Wiebe, 40
- Sitnova, T. M., Yakovleva, S. A., Belyaev, A. K., & Mashonkina, L. I. 2020, *Astron. Lett.*, **46**, 120
- Sitnova, T. M., Yakovleva, S. A., Belyaev, A. K., & Mashonkina, L. I. 2022, *MNRAS*, **515**, 1510
- Skúladóttir, Á., Hansen, C. J., Choplin, A., et al. 2020, *A&A*, **634**, A84
- Sneden, C., Cowan, J. J., Lawler, J. E., et al. 2003, *ApJ*, **591**, 936
- Spite, F., & Spite, M. 1979, *The Messenger*, **16**, 7
- Starkenburger, E., Martin, N., Youakim, K., et al. 2017, *MNRAS*, **471**, 2587
- Takeda, Y., Hashimoto, O., Taguchi, H., et al. 2005, *PASJ*, **57**, 751
- Thomas, G. F., & Battaglia, G. 2022, *A&A*, **660**, A29
- Travaglio, C., Gallino, R., Arnone, E., et al. 2004, *ApJ*, **601**, 864
- Tsybal, V., Ryabchikova, T., & Sitnova, T. 2019, *ASP Conf. Ser.*, **518**, 247
- Ural, U., Cescutti, G., Koch, A., et al. 2015, *MNRAS*, **449**, 761
- Velichko, A. B., Mashonkina, L. I., & Nilsson, H. 2010, *Astron. Lett.*, **36**, 664
- Vieytes, M. C., & Fontenla, J. M. 2013, *ApJ*, **769**, 103
- Wang, S., Necib, L., Ji, A. P., et al. 2023, *ApJ*, **955**, 129
- Wright, J. T., & Eastman, J. D. 2014, *PASP*, **126**, 838
- Xu, X., Shi, J., & Wang, X. 2022, *ApJ*, **936**, 4
- Yakovleva, S. A., Belyaev, A. K., & Mashonkina, L. I. 2022, *Atoms*, **10**, 1
- Yam, W., Carlin, J. L., Newberg, H. J., et al. 2013, *ApJ*, **776**, 133
- York, D. G., Adelman, J., Anderson, John E., J., et al. 2000, *AJ*, **120**, 1579
- Yuan, Z., Smith, M. C., Xue, X.-X., et al. 2019, *ApJ*, **881**, 164
- Yuan, Z., Malhan, K., Sestito, F., et al. 2022, *ApJ*, **930**, 103
- Zhao, G., Zhao, Y.-H., Chu, Y.-Q., Jing, Y.-P., & Deng, L.-C. 2012, *Res. Astron. Astrophys.*, **12**, 723
- Zhao, G., Mashonkina, L., Yan, H. L., et al. 2016, *ApJ*, **833**, 225

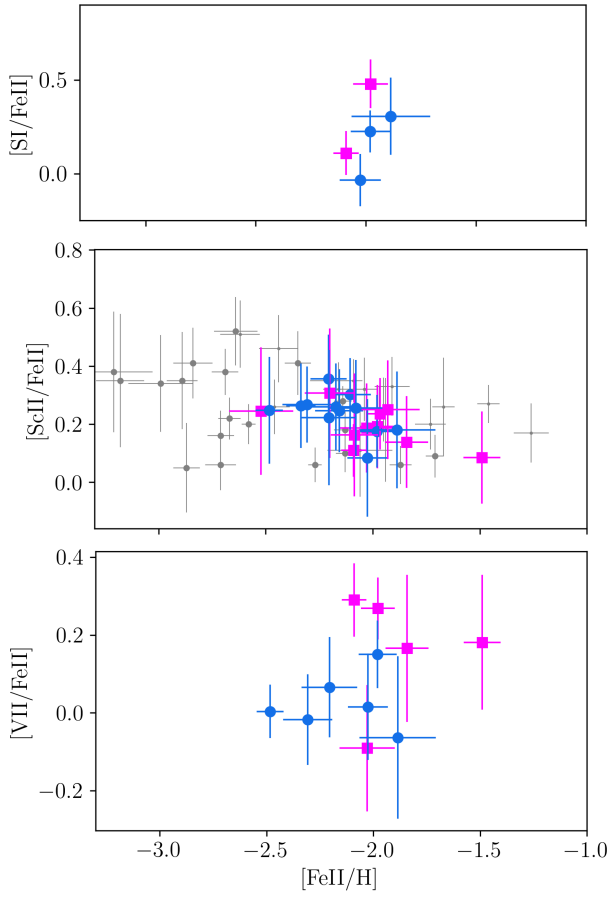


Fig. A.1. Chemical element abundance ratios with respect to iron. The designations are the same as in Fig. 8.

Appendix A: [X/Fe] – [Fe/H] diagrams for the abundance ratios not discussed in the main text

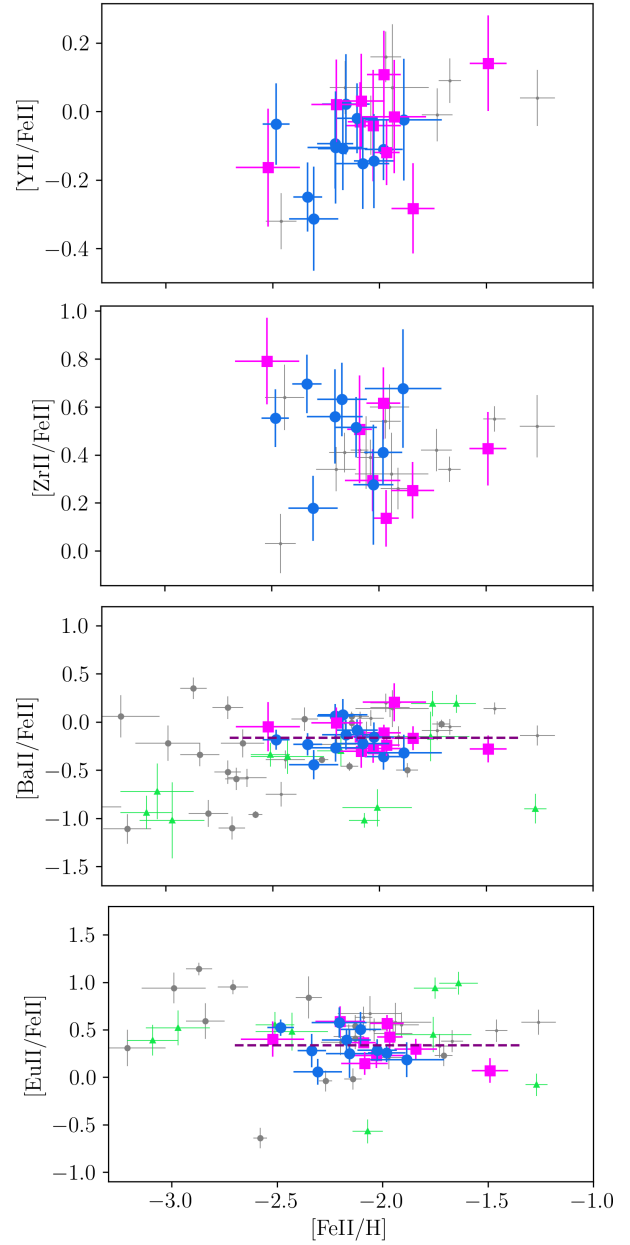


Fig. A.2. Chemical element abundance ratios with respect to iron. The designations are the same as in Fig. 8.